Shen, J., Groh, R., Schenk, M., & Pirrera, A. (2021). Experimental Path-Following of Equilibria Using Newton's Method, Part I: Theory, Modelling, Experiments. *International Journal of Solids and Structures*, *210–211*, 203-223. https://doi.org/10.1016/j.ijsolstr.2020.11.037

Experimental Path-Following of Equilibria Using Newton's Method. Part I: Theory, Modelling, Experiments

J. Shen[a,*], R. M. J. Groh[a], M. Schenk[a], A. Pirrera[a]

[a]*Bristol Composites Institute (ACCIS), University of Bristol, Queen's Building, University Walk, Bristol, BS8 1TR, UK*

Abstract

Modern numerical path-following techniques provide a comprehensive suite of computational tools to study the bifurcation behaviour of engineering structures. In contrast, experimental testing of load-bearing nonlinear structures is still performed using simple force control (dead loading) or displacement control (rigid loading). This means that established experimental methods cannot trace equilibrium manifolds in their entirety because structures snap to alternative equilibria at limit points in the forcing parameter and because branch switching to alternative equilibria cannot be controlled and performed reliably. To extend current testing methods, in Part I of this paper, we implement an experimental path-following method that uses tangent quantities (stiffness and residual forces) and Newton's method to continue along stable and unstable equilibrium paths and traverse limit points. In addition to enforcing the displacement at primary load-introduction points, the overall shape of the structure is controlled via secondary actuators and sensors. Small perturbations of the structure using the secondary actuators allow an experimental tangent stiffness to be computed, which is then used in a control algorithm. As a pertinent test case, the experimental method is applied to a transversely loaded shallow circular arch. Due to the complexity of the test setup, the experiment is first designed using a virtual testing environment based on a surrogate finite element model. Experimental results demonstrate the robustness of the proposed experimental method and the usefulness of virtual testing as a surrogate, but also highlight that experimental efficiency and the effects of noise and sensor uncertainty is of

particular concern. In Part II, we present perspectives on future research directions and novel testing capabilities that are enabled by extending the methodology to pinpointing of critical points, tracing of critical boundaries, and branch switching.

Keywords: experimental path-following, experimental Newton's method, nonlinear structures

1. Introduction

Structural lightweighting is a design driver in many engineering applications. For instance, lighter aircraft are more fuel efficient, and are thus more economical for airlines and less damaging to the environment. However, it is well known that lightweighting and optimisation can be 'generators of instability' [1]. In extreme cases these design strategies lead to 'naive optimisation', whereby a structure that is optimised to fail with simultaneously occurring failure modes becomes sensitive to imperfections and fails much earlier than expected. Similarly, the objective to reduce mass typically leads to thin-walled monocoque structures that are susceptible to buckling instabilities. Common effects of instabilities are reductions in stiffness, sudden drops in load-carrying capacity, or large undesired deflections. Hence, the focus of engineers has generally been to prevent instabilities in order to avoid potentially catastrophic consequences.

Over the last decade, an alternative perspective has developed that treats 'well-behaved nonlinearities' [2] and elastic instabilities as opportunities for additional functionality. In this manner, the traditional (negative) notion of 'buckliphopia' is juxtaposed with a contemporary (positive) view of 'buckliphilia' [3]. In the realm of buckliphilia, buckling has been used for applications as diverse as energy harvesting [4, 5], reversible shape-adaptation [6, 7], surface texturing [8], actuation [9], self-encapsulation [10], auxetic materials [11], and energy dissipation [12].

*Corresponding author: j.shen@bristol.ac.uk

The physics of structural instability is driven by bifurcations, either saddle-node (limit point) or branching (pitchfork/transcritical) bifurcations. In particular, the limit point plays a special role in governing the instability of real (imperfect) engineering structures. In engineering applications, the response of a structure is characterised by equilibrium curves of force *vs* a chosen metric of the displacement field. When the structure reaches a limit point in the loading parameter (force or displacement), its stability changes—a previously stable equilibrium becomes unstable, or *vice versa*. This means that in a structure that is loaded by a slowly evolving, yet monotonously increasing load (force or displacement), an instability triggers a dynamic event upon reaching a limit point, thereby causing the structure to 'snap' to another equilibrium state. Although the force(s) or displacement(s) at the loading point(s) is(are) prescribed, the rest of the structure is free to move dynamically, and this facilitates either additional functionality (*e.g.* shape adaptation) or the loss of functionality (*e.g.* collapse).

Numerous numerical methods have been developed to detect and traverse limit points in an analytical environment. A common method, broadly classified under *numerical path-following* (or *numerical continuation*), is based on the predictor-corrector scheme of Newton's method. To traverse limit points, force(s) and displacement(s) is(are) decoupled at the main load-introduction point(s) by introducing an arc-length constraint equation [13, 14]. Additionally, more advanced path-following algorithms coupled to finite element (FE) solvers can: detect branching points, branch switch to additional equilibrium branches, and trace the loci of limit and branching points in parameter space [2, 15].

In contrast, progress in experimental testing of nonlinear structures is significantly lagging behind numerical methods. The standard quasi-static experimental methods—displacement and force control—break down at the first limit point of the respective loading parameter, thereby leaving parts of the force-displacement equilibrium curve experimentally inaccessible (see Fig. 1). As a result, many classic FE problems (e.g. [16]) remain experimen-

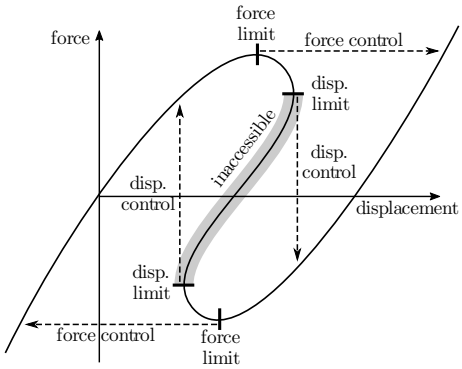

Figure 1: The limits of force- and displacement-controlled test methods.

tally unverified even though they have been used as computational benchmark problems for decades [17]. Moreover, experimental output data are limited to displacements and reaction forces at the main actuation points, and/or deformations at specific points where additional sensors (*e.g.* strain gauges) are placed. Additional quantities, such as the tangent stiffness matrix, which is useful for ascertaining information about the nonlinear behaviour of the structure and intrinsic bifurcation properties, are not available. Finally, researchers working on well-behaved nonlinear structures [2, 6] lack the experimental methods to verify the full mechanical behaviour of their designs. One particularly instructive example are morphing (shape-changing) structures for the aerospace industry, which must meet stringent requirements for commercial certification. While the growing research interest into morphing aerospace structures has led to a plethora of concepts and prototypes [18], very few designs have made their way onto flying aircraft.

The motivation for this work is to level the capabilities between numerical and experimental methods, *i.e.* between analysing/designing and testing/validating nonlinear structures. In this regard, an analogue technique to nonlinear numerical methods, *i.e.* an 'experimental path-following' technique, can provide researchers with a platform to validate concepts experimentally and bring these a step closer to industrial implementation.

In recent years, a number of innovative experimental methods have been developed to

explore the stability of nonlinear structures. Wiebe and Virgin [19] used hammer impacts to trigger the dynamic snap-through of a shallow arch, and were able to infer the location of unstable equilibria from the saddles visible in the arch's dynamic phase space. While this method does not require *a priori* information about the structure being tested, the experiment must be performed multiple times to capture the full range of behaviours. Furthermore, the large dynamic deformations incurred may not be desirable when testing expensive, large-scale components. Virot *et al.* [20] used a 'poker' to laterally perturb an axially loaded cylinder. This particular technique was chosen to detect unstable edge states surrounding the stable pre-buckling equilibrium. An unstable equilibrium was found when the reaction force on the probe vanished; this condition being equivalent to the unprobed cylinder. Because the poker could only push, and not pull, the cylinder could not be held on the unstable edge state, and hence path-following of the unstable equilibrium with varying axial compression was not possible. Van Iderstein and Wiebe [21] stabilised the unstable equilibria of a curved beam, which was buckled into shape using an axial load. Generally speaking, a post-buckled beam can snap-through symmetrically or asymmetrically when loaded by a transverse load. Under displacement-controlled transverse loading, the asymmetric snap-through configuration is stable for most arch geometries and can be observed in practice. By introducing additional control points and implementing a control algorithm based on an experimental 'tangent stiffness matrix', the unstable symmetric path was also traced. However, their particular implementation of the control algorithm breaks down at a displacement limit point where the tangent stiffness becomes singular.

The present authors recently presented an experimental path-following technique [22] based on the concept of 'shape control' [23]. A shallow arch was loaded via rigid loading (displacement control) at the mid-span (main actuation point), while the overall shape of the structure was controlled via two coupled probe points at the quarter- and three-quarter span. The main actuation point was used to step away from a known equilibrium. The

coupled control points were then moved upwards/downwards until a new equilibrium was found—identified by a zero reaction force reading. This rudimentary 'step-scan' approach can traverse displacement limit points and path-follow unstable equilibria, but has certain limitations. Namely, with increasing structural complexity (*e.g.* from arch to shell), the number of probe points to control the structure increases correspondingly. Therefore, a practical experimental path-following setup under these circumstances requires a more sophisticated control algorithm; ideally, one that moves a set of control points concertedly based on the non-zero reaction force readings at all probe points, *i.e.* an experimental analogue to numerical path-following.

In the related yet distinct field of structural dynamics, Sieber *et al.* [24, 25] have developed the methodology known as Control-Based Continuation (CBC). CBC allows dynamic continuation of periodic orbits through a fold, *i.e.* tracking of stable and unstable orbits, and thereby permits tracing of the full nonlinear backbone curve beyond a resonance peak. These methods rely on computing the Jacobian of the root-finding control signal. Ways to estimate the Jacobian in the naturally noisy environment of experiments are discussed by Schilder *et al.* [26] and Renson *et al.* [27, 28].

The work presented in this multi-part paper establishes the same capability but in the field of statics, *i.e.* tracing of equilibria or stationary solutions. We generalise the use of shape control to compute an experimental tangent stiffness matrix. By choosing pertinent control algorithms based on Newton's method, the experimental stiffness matrix allows (i) path-following of stable and unstable equilibria, including traversal of limit points; and (ii) detailed stability analyses such as pinpointing of critical (singular) points, branch switching to alternative equilibrium paths, and tracing of critical points through parameter space. With this approach, many of the features of numerical path-following of stationary solutions can be replicated experimentally. In particular, Part I of this paper focuses on point (i) above: path-following of stable and unstable equilibria and traversal of limit points. Control

algorithms tailored to detailed stability analyses (point (ii) above) are addressed in Part II [29].

The remainder of Part I is structured as follows. Section 2 provides a brief explanation of the concept of shape control and outlines the control algorithms used to path-follow stable and unstable equilibria and traverse limit points. To determine optimal control parameters for robust path-following, we introduce a 'virtual testing' environment in Section 3. The virtual testing environment uses an FE surrogate of the experiment (*e.g.* in ABAQUS) and facilitates designing of the experiment by elucidating the effects of experimental noise and optimal location of control points. Section 4 considers practical challenges in implementing a robust control algorithm based on the experimental tangent stiffness. In Section 5 we demonstrate an experiment of the developed algorithms using a transversely loaded shallow arch and compare the results to our simulations of the experiment. Sources of experimental error and the effect of noise and sensor uncertainty during the experiments is discussed in Section 6 before conclusions are drawn in Section 7.

2. Theory

Before outlining the details of the control algorithms for experimental path-following, we revisit the principles of shape control, previously introduced in [23].

2.1. Shape Control

To illustrate the underlying concepts of shape control, we employ a simple structure that exhibits the salient features of nonlinear behaviour with limit points: the *von Mises* truss connected in series with linear springs (Fig. 2). This structure features an arch-like arrangement of two inclined linear springs, with a third spring suspended from the apex (Fig. 2b). For a load applied to the bottom of the vertical spring (denoted as actuation point a), the force-displacement (F_a *vs* u_a) response describes a general sigmoidal shape. The characteristics of this sigmoidal equilibrium curve are defined by the geometric arrangement (inclina-

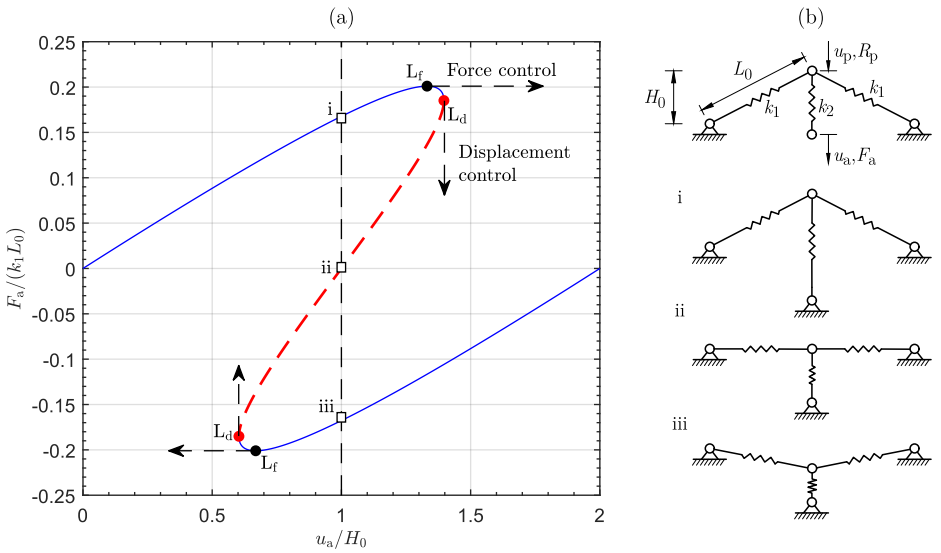

Figure 2: (a) The equilibrium path of the *von Mises* truss connected in series with linear springs with the geometry presented in (b) with the spring ratio $k_1/k_2 = 2$ and $H_0/L_0 = 4/5$. Solid circles labelled with $\mathrm{L_f}$ and $\mathrm{L_d}$ represent force and displacement limit points, respectively. The equilibrium path with a red dashed line is unstable under either force or displacement control. The central section of the plot highlights three equilibria (points i, ii, and iii) with the same actuation displacement ($u_a/H_0 = 1$) but different reaction forces. (c) The truss deformation shapes with the same actuation displacement $u_a/H_0 = 1$ corresponding to points i, ii and iii in (a). Note that F_a and u_a in (b) represent the force and displacement applied on the actuation point in force-controlled loading and displacement-controlled loading respectively; R_p and u_p are the reaction force and displacement at the probe point.

tion α_0, and spring-length L_0) and stiffness ratio of the inclined *vs* vertical springs (k_1/k_2). For certain arrangements, the equilibrium curve features both force and displacement limit points (see Fig. 2a).

With reference to Fig. 2a, under force control, the truss snaps dynamically upon reaching the force limit points L_f. With a displacement-controlled testing method, the portion of the equilibrium path that can be measured extends to the limit points L_d. Hence, using conventional testing techniques, the best one can achieve is to trace the solid lines. Conversely, the statically unstable dashed segment remains experimentally inaccessible. To path-follow along the entire equilibrium manifold, a method for simultaneously controlling the force and displacement at the actuation point is needed. The experimental challenge is

that force and displacement are inherently linked through elasticity: an applied force results in a displacement, and an applied displacement induces a reaction force.

For an applied actuation point displacement of $u_a/H_0 = 1$, the *von Mises* truss features three equilibria, highlighted as i, ii, and iii in Fig. 2a, with different reaction force readings F_a. What differentiates the three reaction force readings is the associated shape of the truss as shown in Fig. 2c. These shapes provide a key insight to experimentally decouple force and displacement at the actuation point; namely, to introduce a third control variable—the overall geometric shape. In a displacement-controlled experiment using any set of actuation points, controlling the equilibrium shape determines the corresponding reaction force(s) at the actuation point(s), and therefore distinguishes between different equilibria on the equilibrium manifold.

The shape of the structure can be readily controlled by introducing additional control points (or so-called 'probe' points). In the case of the *von Mises* truss, the probe point p controls the displacement of the apex (u_p). Hence, each unique equilibrium of the truss is determined by the position of the actuation point (u_a) *and* the relative position of apex and actuation point. For clarity, u_a and u_p are indicated in Fig. 2b.

The purpose of the probe point is threefold. First, the probe stabilises statically unstable equilibria by providing the stabilising reaction force against perturbations. Second, the probe position can be used to select different equilibria that exist for a fixed actuation displacement; Each unique equilibrium state of the unprobed structure must correspond to zero reaction force at the probe ($F_p = 0$). Finally, apart from the zero-force control signal, the probe can be used to evaluate an experimental tangent stiffness matrix.

2.2. Experimental Path-following Algorithm using Tangent Quantities

In numerical path-following, variables are typically divided into *state variables*, $\boldsymbol{u}$, that describe the configuration of the system, and *forcing parameters*, $\boldsymbol{\Lambda}$, which control the state. In classic finite element solvers with displacement degrees-of-freedom (dofs), the state is

given by the displacements (and sometimes rotations) at the discretisation nodes, and the forcing parameters are the applied forces and tractions (which are generally converted into nodal forces and moments). However, it is also possible that one of the state variables becomes an active parameter that controls the other state variables. This is the case in rigid (displacement-controlled) loading, which is often chosen in experimental settings.

For experimental path-following using displacement-controlled inputs, it is therefore convenient to let the state $\boldsymbol{u}$ be a vector of displacements at N specified control points (N_a main actuation points plus N_p probing control points). These points are analogous to nodes in a finite element setting as their position can be controlled to define the global shape of the structure. Initially, we focus on a single-parameter system such that the parameter set $\boldsymbol{\Lambda}$ becomes a single scalar variable λ. The displacements at the main actuation points (actual loading of the unprobed structure) are henceforth denoted by $\boldsymbol{u}_\mathrm{a}$, and the displacements at the probing control points (to stabilise unstable equilibria and control the overall shape) are denoted by $\boldsymbol{u}_\mathrm{p}$. Thus, $\boldsymbol{u} = [\boldsymbol{u}_\mathrm{p}^\top \ \boldsymbol{u}_\mathrm{a}^\top]^\top$.

For a conservative structural system, an equilibrium state is given by a balance of the internal forces, $\boldsymbol{f}_\mathrm{int}$, and the external forces, $\boldsymbol{f}_\mathrm{ext}$. Analogous to the state variables, $\boldsymbol{u}$, the internal and external forces are vectors that describe the respective forces at the specified control points ('nodes'). Equilibrium is obtained when all externally applied forces at control points are equal to the internal loads, *i.e.* the residual vanishes:

$$\boldsymbol{R}(\boldsymbol{u}, \lambda) = \boldsymbol{f}_\mathrm{int}(\boldsymbol{u}) - \boldsymbol{f}_\mathrm{ext}(\lambda) = \boldsymbol{0}. \tag{1}$$

Formally speaking, except passive reaction forces, no external active forces are applied in a displacement-controlled experimental path-following setup ($\boldsymbol{f}_\mathrm{ext} \equiv \boldsymbol{0}$). However, at all main actuation points, a reaction force is naturally induced when non-zero displacements are applied, and these reaction forces play the role of external forces in the algorithm. The displacements at the main actuation points are therefore defined implicitly through the

forcing parameter λ. Specifically, the displacements at the main actuation points, $\boldsymbol{u}_\mathrm{a}$, are expressed as the product of an unchanging reference displacement vector, $\hat{\boldsymbol{u}}_\mathrm{a}$, and a changing scalar variable, λ. Hence, $\boldsymbol{u}_\mathrm{a} = \lambda\hat{\boldsymbol{u}}_\mathrm{a}$.

For the displacement-controlled system, each equilibrium configuration is defined by non-zero internal forces at the main actuation points and zero internal forces at all probing control points. Therefore, the unique identifier of an equilibrium state is the vanishing of the control forces at all probing control points

$$\boldsymbol{R}_\mathrm{p}(\boldsymbol{u}_\mathrm{p}, \boldsymbol{u}_\mathrm{a}(\lambda)) = \boldsymbol{f}^\mathrm{p}_\mathrm{ctrl}(\boldsymbol{u}_\mathrm{p}, \boldsymbol{u}_\mathrm{a}(\lambda))=\boldsymbol{0}. \tag{2}$$

Because $\boldsymbol{R}_\mathrm{p}$ is generally non-linear in $\boldsymbol{u} = (\boldsymbol{u}_\mathrm{p}, \boldsymbol{u}_\mathrm{a}(\lambda))$, we linearise the system to give

$$\boldsymbol{R}_\mathrm{p}(\boldsymbol{u}_\mathrm{p} + \Delta\boldsymbol{u}_\mathrm{p}, \lambda + \Delta\lambda) = \boldsymbol{R}_\mathrm{p}(\boldsymbol{u}_\mathrm{p}, \boldsymbol{u}_\mathrm{a}(\lambda)) + \frac{\partial \boldsymbol{R}_\mathrm{p}}{\partial \boldsymbol{u}_\mathrm{p}}\Delta\boldsymbol{u}_\mathrm{p} + \frac{\partial \boldsymbol{R}_\mathrm{p}}{\partial \lambda}\Delta\lambda + \cdots = \boldsymbol{0}. \tag{3}$$

To a first-order approximation Eq. (3) reads

$$\frac{\partial \boldsymbol{R}_\mathrm{p}}{\partial \boldsymbol{u}_\mathrm{p}}\Delta\boldsymbol{u}_\mathrm{p} + \frac{\partial \boldsymbol{R}_\mathrm{p}}{\partial \lambda}\Delta\lambda = -\boldsymbol{R}_\mathrm{p}(\boldsymbol{u}_\mathrm{p}, \boldsymbol{u}_\mathrm{a}(\lambda)). \tag{4}$$

At an equilibrium state $\boldsymbol{R}_\mathrm{p}$ is zero. But for any non-equilibrium state stabilised by the probing control points $\boldsymbol{R}_\mathrm{p}$ is non-zero. Next, we consider the significance of the partial derivatives in Eq. (4). In the first term,

$$\frac{\partial \boldsymbol{R}_\mathrm{p}}{\partial \boldsymbol{u}_\mathrm{p}} = \frac{\partial \boldsymbol{f}^\mathrm{p}_\mathrm{ctrl}}{\partial \boldsymbol{u}_\mathrm{p}} = \boldsymbol{K}^\mathrm{pp}_\mathrm{T}, \tag{5}$$

which is the $N_\mathrm{p} \times N_\mathrm{p}$ *direct* tangent stiffness matrix relating tangent probe reaction forces to incremental displacements at the probes. In the second term,

$$\frac{\partial \boldsymbol{R}_\mathrm{p}}{\partial \lambda} = \frac{\partial \boldsymbol{f}^\mathrm{p}_\mathrm{ctrl}}{\partial \lambda} = \frac{\partial \boldsymbol{f}^\mathrm{p}_\mathrm{ctrl}}{\partial \boldsymbol{u}_\mathrm{a}}\frac{\partial \boldsymbol{u}_\mathrm{a}}{\partial \lambda} = \boldsymbol{K}^\mathrm{pa}_\mathrm{T}\hat{\boldsymbol{u}}_\mathrm{a}, \tag{6}$$

is a column vector of tangential forces induced by the reference displacement vector $\hat{\boldsymbol{u}}_\mathrm{a}$. The $N_\mathrm{p} \times N_\mathrm{a}$ *coupling* tangent stiffness matrix $\boldsymbol{K}^\mathrm{pa}_\mathrm{T}$ captures the tangent probe reaction forces

induced by incremental displacements at the main actuation points. In aggregate, the *total* probing tangent stiffness matrix of size $N_\mathrm{p} \times (N_\mathrm{p} + N_\mathrm{a})$ is given by

$$\boldsymbol{K}_\mathrm{T}^\mathrm{p} = \begin{bmatrix} \boldsymbol{K}_\mathrm{T}^\mathrm{pp} & \boldsymbol{K}_\mathrm{T}^\mathrm{pa} \end{bmatrix}. \tag{7}$$

In a numerical setting, the tangent stiffness matrix $\boldsymbol{K}_\mathrm{T}^\mathrm{p}$ can be computed in two ways: (i) the partial derivative of the internal forces can be computed analytically such that tangent stiffness is computed exactly; or (ii) a finite difference approximation can be used. For the latter, the ith column of the tangent stiffness matrix is given by

$$\boldsymbol{K}_\mathrm{T}^{\mathrm{p},i} \approx \frac{\boldsymbol{f}_\mathrm{ctrl}^\mathrm{p}(\boldsymbol{u} + \epsilon\|\boldsymbol{u}\|_2 \boldsymbol{e}^i) - \boldsymbol{f}_\mathrm{ctrl}^\mathrm{p}(\boldsymbol{u})}{\epsilon\|\boldsymbol{u}\|_2}, \tag{8}$$

where $\boldsymbol{e}^i$ is a column vector with the ith component equal to unity and the rest equal to zero, ϵ is a small scalar, and $\|\boldsymbol{u}\|_2$ is the L2-norm of the displacement vector, *i.e.* $\|\boldsymbol{u}\|_2 = (\boldsymbol{u}\cdot\boldsymbol{u})^{1/2}$.

Because an analytical expression of the tangent stiffness matrix is not generally available in an experimental setting, we compute $\boldsymbol{K}_\mathrm{T}^\mathrm{p}$ using the finite difference approximation of Eq. (8). In practice, this means that the ith control point in the total set of main actuation points plus probing control points is displaced in turn by a small amount $\epsilon\|\boldsymbol{u}\|_2$ and the resulting internal forces (reaction forces) at the probing control points are measured. The corresponding column of the tangent stiffness matrix is then computed by subtracting the unperturbed reaction forces from these perturbed reaction forces and dividing by the small perturbation $\epsilon\|\boldsymbol{u}\|_2$. By repeating this procedure for each control point ($i = 1 \ldots N$), an experimental tangent stiffness matrix is assembled. Note that this procedure relies on the assumption that the supports for the actuation points and probes are infinitely stiff and do not deflect under the applied reaction loads.

Using the definition of the direct and coupling tangent stiffness matrices of Eqs. (5)

and (6), and the implicit definition of $\boldsymbol{u}_{\mathrm{a}}(\lambda)$, we now rewrite Eq. (4) as follows:

$$\boldsymbol{K}_{\mathrm{T}}^{\mathrm{pp}}\Delta\boldsymbol{u}_{\mathrm{p}} + \boldsymbol{K}_{\mathrm{T}}^{\mathrm{pa}}\hat{\boldsymbol{u}}_{\mathrm{a}}\Delta\lambda = -\boldsymbol{R}_{\mathrm{p}}(\boldsymbol{u}_{\mathrm{p}}, \lambda). \tag{9}$$

Equation (9) is solved by the control algorithm to increment away from a known equilibrium with $\boldsymbol{R}_{\mathrm{p}} = \boldsymbol{0}$ (the predictor) and to iterate towards a new equilibrium with $\boldsymbol{R}_{\mathrm{p}} \neq \boldsymbol{0}$ (the corrector).

Because the N_{p} equations in (9) have $N_{\mathrm{p}} + 1$ unknown quantities—N_{p} displacement increments of the probing points, $\Delta\boldsymbol{u}_{\mathrm{p}}$, and one displacement increment of the main actuation points, $\Delta\lambda$—an additional bordering equation is required to solve the linearised equilibrium equation. This equation can take many forms but the critical requirement is traversal of limit points. Following Riks [13], we use the simplest linear bordering equation

$$\Delta\boldsymbol{u}_{\mathrm{p}}^{(1,k)} \cdot \Delta\boldsymbol{u}_{\mathrm{p}}^{(j,k)} + \beta^2\Delta\lambda^{(1,k)}\Delta\lambda^{(j,k)} = 0, \tag{10}$$

where the dot refers to the scalar product, the superscript $\bullet^{(1,k)}$ denotes the linear predictor for load step k away from the converged equilibrium of load step $k-1$, and the superscript $\bullet^{(j,k)}$ denotes the jth corrector iteration towards a new equilibrium of load step k. The scalar β is a quantity that can be used to modify the relative magnitude of the probe and actuation point displacements in the corrector.

Equations (9) and (10) can now be combined to solve for any equilibrium $(\Delta\boldsymbol{u}_{\mathrm{p}}^{(j,k)}, \Delta\lambda^{(j,k)})$. Following standard practice of numerical path-following [30], the control algorithm performs this task most efficiently by splitting the increment at the probing control points into two components: (i) $d\boldsymbol{u}_{\mathrm{p}}$, which is a corrector displacement arising from the residual $\boldsymbol{R}_{\mathrm{p}}$, and (ii) $\delta\boldsymbol{u}_{\mathrm{p}}$, which is the 'tangential' probe displacement arising from the applied displacements at the main actuation points. Namely, solving Eq. (9) for $\Delta\boldsymbol{u}_{\mathrm{p}}$ gives

$$\Delta\boldsymbol{u}_{\mathrm{p}}^{(j,k)} = d\boldsymbol{u}_{\mathrm{p}}^{(j,k)} + \Delta\lambda^{(j,k)} \cdot \delta\boldsymbol{u}_{\mathrm{p}}^{(j,k)}, \tag{11}$$

where

$$d\boldsymbol{u}_{\mathrm{p}}^{(j,k)} = -\boldsymbol{K}_{\mathrm{T}}^{\mathrm{pp}^{-1}} \boldsymbol{R}_{\mathrm{p}}^{(j,k)}, \tag{12}$$

$$\delta\boldsymbol{u}_{\mathrm{p}}^{(j,k)} = -\boldsymbol{K}_{\mathrm{T}}^{\mathrm{pp}^{-1}} \boldsymbol{K}_{\mathrm{T}}^{\mathrm{pa}} \hat{\boldsymbol{u}}_{\mathrm{a}}. \tag{13}$$

The tangent stiffness components $\boldsymbol{K}_{\mathrm{T}}^{\mathrm{pp}}$ and $\boldsymbol{K}_{\mathrm{T}}^{\mathrm{pa}}$ can be updated at every iteration (j,k), *i.e.* full Newton method, or only at the beginning of each load step $(1,k)$, *i.e.* modified Newton method. During the experiments, the finite difference procedure to compute $\boldsymbol{K}_{\mathrm{T}}^{\mathrm{pp}}$ and $\boldsymbol{K}_{\mathrm{T}}^{\mathrm{pa}}$ was found to be the greatest time investment, such that the modified approach was used.

It may be assumed that the previous load step has converged to a small tolerance, such that $\boldsymbol{R}_{\mathrm{p}}^{(1,k)} = \boldsymbol{0}$. Therefore, only $\delta\boldsymbol{u}_{\mathrm{p}}$ needs to be solved for the first increment of any load step (the predictor). In this case, a value for $\Delta\lambda^{(1,k)}$ is prescribed based on a desired arc-length, Δs:

$$\Delta s^2 = \Delta\boldsymbol{u}_{\mathrm{p}} \cdot \Delta\boldsymbol{u}_{\mathrm{p}} + \beta^2 \Delta\lambda^2. \tag{14}$$

Thus, for a specific defined arc-length, the predictor increment can be computed from

$$\Delta\lambda^{(1,k)} = \frac{\Delta s}{\sqrt{\delta\boldsymbol{u}_{\mathrm{p}}^{(1,k)} \cdot \delta\boldsymbol{u}_{\mathrm{p}}^{(1,k)} + \beta^2}}, \tag{15}$$

where $\delta\boldsymbol{u}_{\mathrm{p}}^{(1,k)}$ is first calculated using Eq. (13). Furthermore, the predictor step size is adapted to the convergence rate of previous load step, *i.e.*

$$\Delta\lambda^{(1,k)} = \left(\frac{n^{(k-1)}}{n^{\mathrm{desired}}}\right)^{0.25} \Delta\lambda^{(1,k-1)}, \tag{16}$$

where $n^{(k-1)}$ is the number of iterations required to converge in the preceding load step $k-1$, and n^{desired} is the desired number of iterations to achieve convergence.

To traverse limit points, the sign of the predictor $\Delta\lambda^{(1,k)}$, and hence the direction of the actuation incremental displacement, $\Delta\boldsymbol{u}_{\mathrm{a}}^{(1,k)} = \Delta\lambda^{(1,k)}\hat{\boldsymbol{u}}_{\mathrm{a}}$, needs to be controlled. This can be achieved by comparing the total displacement increment of the probes (predictor

plus correctors) in the previous load step, $\Delta \boldsymbol{u}_{\mathrm{p}}^{(k-1)}$, with the current 'tangential' probe displacement predictor $\delta \boldsymbol{u}_{\mathrm{p}}^{(1,k)}$. If these two vector quantities point in the same direction, then the movement direction of the actuation points, $\Delta \boldsymbol{u}_{\mathrm{a}}^{(1,k)}$, remains the same. Otherwise the direction is reversed. Hence,

$$\begin{aligned} &\textbf{if } \Delta \boldsymbol{u}_{\mathrm{p}}^{(k-1)} \cdot \delta \boldsymbol{u}_{\mathrm{p}}^{(1,k)} > 0 \\ &\qquad \Delta \lambda^{(1,k)} = \|\Delta \lambda^{(1,k)}\|_2 \\ &\textbf{else} \\ &\qquad \Delta \lambda^{(1,k)} = -\|\Delta \lambda^{(1,k)}\|_2, \end{aligned} \tag{17}$$

where $\Delta \lambda^{(1,k)}$ has first been determined using Eq. (15).

At the end of the predictor increment, the incremental displacements $(\Delta \boldsymbol{u}_{\mathrm{p}}^{(1,k)}, \Delta \boldsymbol{u}_{\mathrm{a}}^{(1,k)})$ are defined such that the main actuation points and probing points can be moved to new positions. Because the predictor is a linear step, this new state is not necessarily an equilibrium, and this manifests as non-zero reaction forces at the probe points ($\boldsymbol{R}_{\mathrm{p}} \neq \boldsymbol{0}$). Hence, the positions of the main actuation points and probing points need to be corrected.

For corrector increments, both $\delta \boldsymbol{u}_{\mathrm{p}}^{(j,k)}$ and $d\boldsymbol{u}_{\mathrm{p}}^{(j,k)}$ are computed and the appropriate $\Delta \lambda^{(j,k)}$ is found using (10). By substituting (11) into (10), we get

$$\Delta \boldsymbol{u}_{\mathrm{p}}^{(1,k)} \cdot \left(d\boldsymbol{u}_{\mathrm{p}}^{(j,k)} + \Delta \lambda^{(j,k)} \delta \boldsymbol{u}_{\mathrm{p}}^{(j,k)} \right) + \beta^2 \Delta \lambda^{(1,k)} \Delta \lambda^{(j,k)} = 0, \tag{18}$$

$$\Delta \lambda^{(j,k)} = -\frac{\Delta \boldsymbol{u}_{\mathrm{p}}^{(1,k)} \cdot d\boldsymbol{u}_{\mathrm{p}}^{(j,k)}}{\Delta \boldsymbol{u}_{\mathrm{p}}^{(1,k)} \cdot \delta \boldsymbol{u}_{\mathrm{p}}^{(j,k)} + \beta^2 \Delta \lambda^{(1,k)}}. \tag{19}$$

The corrector sequence iteratively applies (11) and (19) for n iterations until the algorithm has converged to a new equilibrium. An equilibrium state is defined by the vanishing of the reaction forces at the probing points. Numerically this is achieved when a norm of all the probe point residuals falls beneath a specific threshold. Hence, $\|\boldsymbol{R}_{\mathrm{p}}\|_2 < R_{\mathrm{p,tol}}$, where $R_{\mathrm{p,tol}}$ is a specified tolerance.

The equations outlined in this section describe a general algorithm for experimental path-

following of stable and unstable equilibria and traversal of limit points. For clarity, step-by-step algorithmic details are elucidated in Appendix A. The algorithm is fundamentally identical to an implementation in an FE setting, with the exception of the necessity of calculating the experimental tangential stiffness matrix through finite differences. Note that in the experiments presented on a transversely loaded shallow arch in Section 5, only one main actuation point and one independent probe exists. In this case, the bold symbols used above to represent vectors and matrices (*e.g.* $\boldsymbol{u}_\mathrm{a}$, $\boldsymbol{u}_\mathrm{p}$, $\boldsymbol{K}_\mathrm{T}^\mathrm{pa}$, $\boldsymbol{K}_\mathrm{T}^\mathrm{pp}$, $\boldsymbol{R}_\mathrm{p}$, *etc.*) will be dropped for roman symbols to reflect the scalar nature of the quantities (*e.g.* u_a, u_p, K_T^pa, K_T^pp, R_p, *etc.* but $\boldsymbol{K}_\mathrm{T}^\mathrm{p} = [K_\mathrm{T}^\mathrm{pp} \; K_\mathrm{T}^\mathrm{pa}]$).

In the following section, we introduce a virtual testing environment based on a surrogate FE model to test the algorithm and determine probe locations that allow for robust experimental path-following of a transversely loaded shallow arch. In Section 4 we present practical modifications made to the controlling algorithm outlined above based on observations made during virtual testing and the experimental testing campaign.

3. Virtual Testing Environment

The testing setup for experimental path-following is considerably more complex than for a traditional approach using force- or displacement-control at one or multiple loading points. For example, the main actuation and probe points need to be moved by independent actuators and a controlling algorithm is required to coordinate the different inputs. For these reasons, a virtual testing environment is valuable as it allows the experimenter to test control algorithms, identify the optimum location of probe points, explore possible issues during the experiment (*e.g.* the influence of noise), and ensure safe operation.

The virtual testing environment with the controlling path-following algorithm is implemented in the FE software Abaqus using Python scripts. Displacement control at the probes and the main actuation point is implemented by imposing nodal displacement.

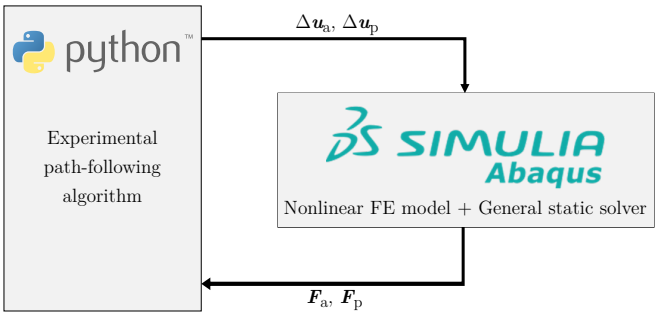

Figure 3: Virtual testing environment. The details of the path-following algorithm can be found in Section 2.2.

ABAQUS' general static solver (nonlinear Newton solver without capability to traverse limit points) is adopted to move the probe and main actuation points under displacement control, thereby also deforming the rest of the arch. Thus, ABAQUS' general static solver acts as a surrogate to simulate how the arch deforms when the probes and main actuations points are moved, and determine the reaction forces expected at these points. The movement of the probing and main actuation control points is synchronised so that the main actuation point displacement can be continuously varied while maintaining zero reaction force on the probe. Specifically, the control logic outlined in the preceding section for path-following of equilibria is implemented in PYTHON scripts, which then control the movements of the control points in ABAQUS, as shown in Figure 3.

To allow ABAQUS to continuously change the boundary conditions that control the positions of the probes and main actuation point, the functionality known as *restart analysis* needs to be adopted. A restart analysis allows a new analysis to continue from the point where a previous analysis left off. This enables us to sequentially apply displacements at the control points as dictated by the path-following control logic, where each increment in the loading process is a new model in the restart analysis.

The test case chosen for the experimental implementation (Section 5) is a shallow circular arch, pinned at two ends and loaded by a transverse mid-span load. Before testing the arch

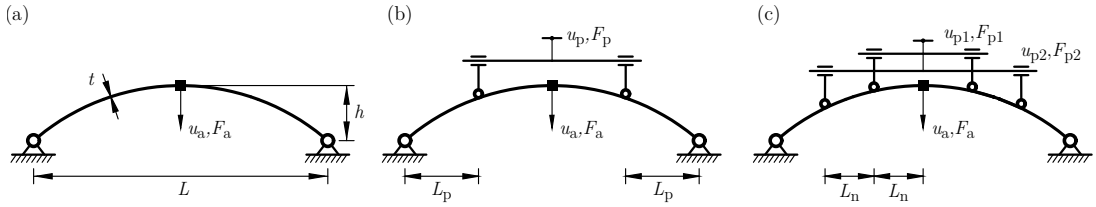

Figure 4: (a) Shallow circular arch studied in this paper. The edges of the arch are pinned. Vertical displacement (u_a) is applied at the mid-span and this displacement induces a reaction force (F_a). Rotations and lateral translations are constrained at the mid-span to preserve symmetry. (b) Additional control points provide shape control while preserving left-right symmetry. A vertical displacement (u_p) is applied symmetrically to the probes at a horizontal distance L_p from the ends. The probes are designed to be minimally invasive to prevent reaction moments and horizontal reaction forces that would perturb the equilibrium path. (c) Arch with multiple pairs of probes. Probes are evenly and symmetrically distributed, where $L_n = L/[2(n+1)]$ and n is the number of probe pairs.

physically, we designed the experiment using the virtual testing environment. The geometry of the arch is presented in Fig. 4a, with dimensions $L = 205\,\text{mm}$, $h = 20\,\text{mm}$, $t = 1.57\,\text{mm}$, and depth $D = 4.68\,\text{mm}$ (into the page). The constituent material is assumed to be linearly elastic, homogeneous and isotropic, with Young's modulus $E = 3200\,\text{MPa}$ and Poisson's ratio $\nu = 0.38$. The arch is modelled using the in-plane linear beam element B21 in ABAQUS, which assumes Timoshenko beam theory.

A transversely loaded shallow arch has the tendency to snap-through asymmetrically, *i.e.* to break left-right symmetry. Here, we focus on symmetric deformation modes because these are sufficient to achieve the aims of this paper; namely, to path-follow stable and unstable equilibria and traverse limit points. Left-right symmetry is enforced by preventing rotations around the mid-span of the arch. In FE this is easily done by enforcing a boundary condition, whereas in the experiments of Section 5 the mid-span point is prevented from rotating using a rigid clamp, and symmetrically placed coupled probes.

Figure 5 shows the equilibrium manifold of the arch as derived from the quasi-static Riks solver implemented in ABAQUS. Note that the equilibrium manifold only shows the

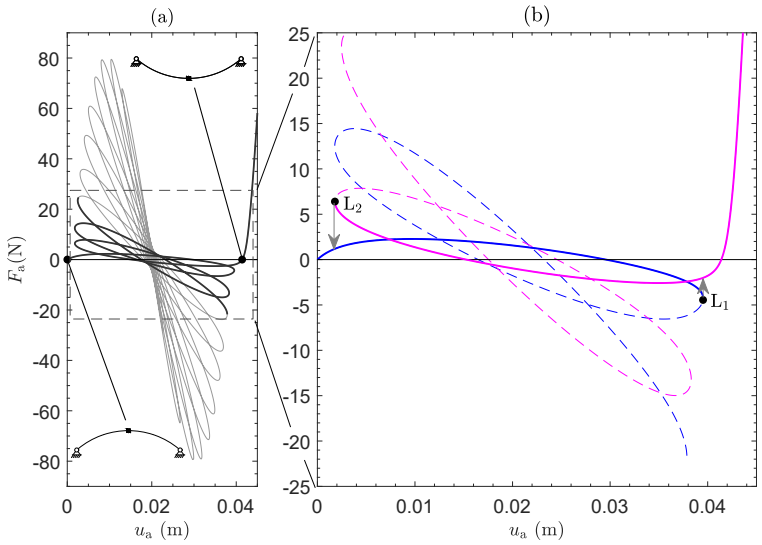

Figure 5: Nonlinear force-displacement equilibrium path of the shallow circular arch solved using the quasi-static Riks solver in ABAQUS. (a) Complete symmetric response. Also shown are the arch shapes corresponding to the undeformed and inverted states. (b) Subset of the response. The solid lines indicate the segments that a conventional displacement-controlled testing protocol can obtain; dashed lines indicate the equilibria that are inaccessible experimentally using standard displacement-controlled testing as they lie beyond displacement limit points. Blue and magenta lines represent loading from the undeformed to the inverted states and *vice versa*, respectively.

'flower petal' path corresponding to symmetric solutions. Symmetry-breaking paths are not shown. A conventional displacement-controlled testing method could only trace a fraction of the predicted response, shown by the solid lines in Fig. 5b. Upon loading from the resting configuration, the arch would snap through into its inverted configuration at displacement limit point L_1. Conversely, upon unloading, the arch would snap back at limit point L_2. The aim of the experiments in Section 5 is to traverse limit points L_1 and L_2. To demonstrate the capabilities of the virtual testing environment, however, it sufficient to focus on one segment of the equilibrium manifold; namely, the blue lines in Fig. 5b.

3.1. Effect of Probe Locations

The layout of the probes is critical for successful implementation of the proposed experimental path-following method, as it determines the fidelity to which the structural shape

can be controlled. Within the virtual testing environment, a parametric study is conducted to evaluate effective probe placement (in pairs to enforce symmetry). Results are shown in Figure 6, where solid lines correspond to quasi-static Riks solutions from ABAQUS (no probes) and square markers denote load step increments computed using the virtual instantiation of the experimental path-following setup (using probes and algorithm in Section 2.2). Figures 6a–f show results for varying probe locations, from closest to furthest away from the pinned supports, respectively. In each case, the final data point—marked by a red cross—denotes the position where the experimental path-following algorithm fails to converge and thus cannot path-follow any further.

All probe locations are capable of accurately replicating the numerical Riks solution from ABAQUS (no probes) and traversing the first displacement limit point. Prior to the limit point, all equilibria are stable and this means that the probes can be removed without causing the arch to snap to another equilibrium (provided that symmetry is prescribed at the mid-span). The equilibria past the limit point, however, are unstable, which means that once the probes are removed, the arch is free to snap to another inherently stable equilibrium. This illustrates the key function of the probes: stabilising unstable equilibria.

Figures 6a–f are produced with identical numerical settings for the path-following algorithm. Although convergence is affected by these settings, a physical limit to what the algorithm can achieve is imposed by the nature of the problem. Physically, the lack of convergence at the red crosses in Fig. 6 corresponds to the instance whence the probe loses control authority to move the structure to the next equilibrium. Hence, more probe points would be required to continue further along the equilibrium manifold; this problem is addressed in further detail in Section 3.2. When the probes are close to the mid-span (and hence to the actuation point), the algorithm struggles to converge immediately after traversing the limit point. This is because the probes lose control authority over the unrestrained portions of the arch, namely the parts between the boundary supports and the probes. Physically, during

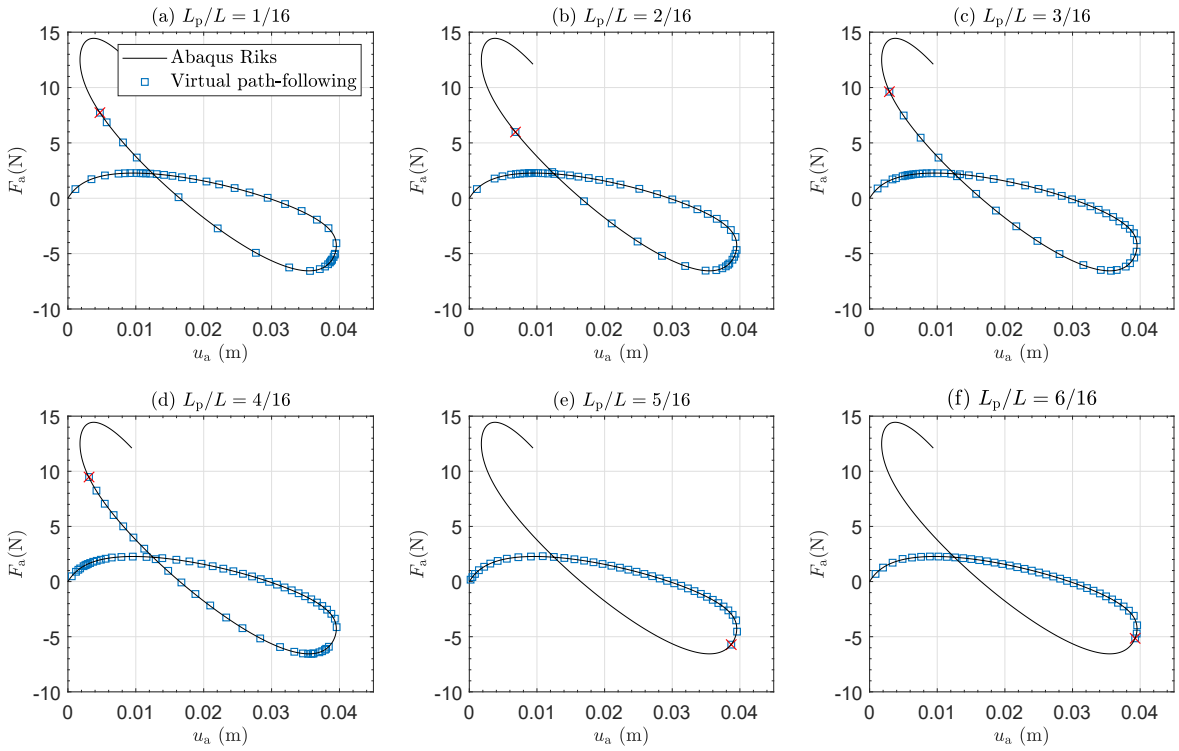

Figure 6: Virtual testing results for cases with different probe locations. The definitions of F_a, u_a and L_p can be found in Fig. 4b. The convergence tolerance for the total residual reaction force at the probes is $R_{p,tol} = 0.1\,N$. The arc-length parameter $\beta = 0$ for all virtual testing in this section. Note that the squares represent the converged equilibria from virtual testing; the solid line represents numerical results obtained using the quasi-static Riks solver in ABAQUS (no probes); and crosses denote the instance where the experimental path-following algorithm fails to progress along the equilibrium path. Identical numerical settings are adopted for the path-following algorithm in (a–f).

the perturbation process to find $\boldsymbol{K}_T^p$, the unrestrained portions of the arch snap through and, once the perturbation is reversed, the arch does not return exactly to its previous equilibrium state, even though the probes return to their original position. This is also observed experimentally in Section 5.

It should be noted that even though the path-following algorithm works well for probe locations $L_p/L \leq 4/16$, there exist portions of the equilibrium curve where the incremental step size is fine. This range corresponds to the displacement turning points of the probes, *i.e.* $K_T^{pa} = 0$, and this problem can be eliminated by adopting a relatively large value for β

in the arc-length equation, more details of which can be found in Appendix B.3.

3.2. Multiple Independent Probes

Test setups with multiple independent probes are simple extensions of the system studied in Section 3.1. With the capability of controlling multiple probes simultaneously, additional displacement limit points along the 'flower-petal' manifold can be traversed.

Here, virtual testing with two and four pairs of probes is conducted (each preserving symmetry about the mid-span). The probes are evenly distributed horizontally, as shown for two pairs of probes in Fig. 4c, and each pair is controlled independently. Figure 7 shows the virtual testing results compared to a quasi-static Riks solution from ABAQUS (no probes). It is evident that, with an increase in the number of probe pairs, more displacement limit points can be traversed; *i.e.* the number of limit points traversed is equal to the number of probe pairs. Due to the ability to traverse additional limit points, high-order deformation modes can be controlled and stabilised. The higher-order modes displayed in Fig. 7 correspond to the last converged load step (red cross).

3.3. Controlling Parameter Sensitivity Study

With the virtual testing environment, we can also conduct sensitivity studies on the effects of primary controlling parameters in the algorithm (such as residual force tolerance at the probes, maximum incremental displacement step size at the controlling points, perturbation size at controlling points to approximate the tangential stiffness matrix) and the effect of measurement noise on experimental continuation so as to design the most feasible and efficient testing scheme. A detailed parameter sensitivity study for experimental continuation of the circular shallow arch can be found in the Supplementary Materials. The key findings can be summarised as follows:

1. Less stringent reaction force tolerance values, $\boldsymbol{R}_{\mathrm{p,tol}}$, can be balanced by decreasing the maximum incremental displacement step size. Hence, if the force sensors on the probes

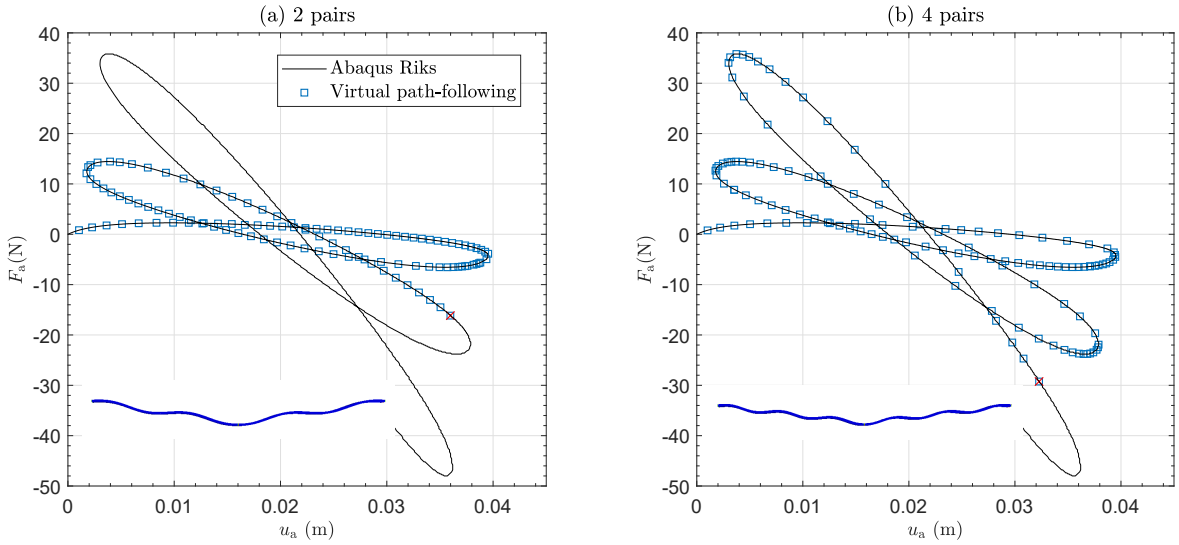

Figure 7: Virtual testing results for (a) two pairs of probes; and (b) four pairs of probes. The convergence tolerance for the reaction force at each pair of probes is $R_{\mathrm{p,tol}} = 0.1\,\mathrm{N}$. Inset are the arch deformations at the last converged load step (red cross) which illustrate the need for multiple probes to control the deformed shape. Note that the probes are evenly distributed, *i.e.* the horizontal distance between the probe pairs is equal, as shown for two probe pairs in Fig. 4c.

have poor measurement accuracy, then the incremental displacement step size should be reduced accordingly. There is, of course, a limit to how small displacement increments can be, due to limitations on actuator precision and backlash in components. Thus, a compromise needs to be established between probe force sensor accuracy and displacement actuator precision. Further trade-offs concern the total duration of an experiment, achieving a balance between the time required to compute the tangent stiffness and to execute the subsequent predictor-corrector steps.

2. To minimise the effect of noise, attention should be placed on the approximation of the tangential stiffness matrix. The reaction force variation during the perturbation process needs to be much larger than experimental noise. The effects of random noise can be decreased by taking the average value of multiple perturbation measurements.
3. A smaller perturbation size leads to a better approximation of the tangential stiffness

matrix (excluding the effects of measurement noise and uncertainty), thus leading to a quicker convergence rate. There exists a lower-bound threshold for the perturbation size below which $\boldsymbol{K}_{\mathrm{T}}^{\mathrm{p}}$ is not affected.

Note that a more thorough discussion based on the experiments can be found in Sections 4 and 5.

3.4. Optimal Probe Layout: Effective Independence Index

The role of probe points is to provide stabilising restraints as well as to monitor the real-time stability characteristics of the structure through the experimental tangent stiffness matrix. As the number of independent probes is increased, the size of $\boldsymbol{K}_{\mathrm{T}}^{\mathrm{pp}}$ increases accordingly, meaning that the control authority over the structure also increases. As a result, a larger set of critical eigenvalues and eigenvectors of the unprobed structure can be stabilised. The layout of the probes should reflect the critical eigenvectors (the eigenvectors corresponding to each zero eigenvalue at critical points) of the unprobed structure's tangent stiffness matrix. Accordingly, it is most effective if the probes are located at the maximum amplitudes of the deformation mode corresponding to each critical eigenvector. As the apexes of different eigenvectors are located at different points over the domain of the structure, a compromise needs to be found that best satisfies the probe placement for all critical eigenvectors.

The effective independence method [31] is adopted to establish the most effect position of the probes for control. The effective independence method was originally proposed to determine the apexes of vibration modes for optimal sensor placement in structural dynamic tests [32, 33]. For effective shape control, the incremental displacement of the probes at displacement limit points, $\Delta\boldsymbol{u}_{\mathrm{p}}^{\mathrm{lp}}$, should satisfy

$$\Delta\boldsymbol{u}_{\mathrm{p}}^{\mathrm{lp}} = \boldsymbol{\Phi}_{\mathrm{fp}}^{0}\boldsymbol{q} = \left[\boldsymbol{\phi}_{\mathrm{lp},1}^{\mathrm{fp}\ \top} \quad \boldsymbol{\phi}_{\mathrm{lp},2}^{\mathrm{fp}\ \top} \quad \cdots \quad \boldsymbol{\phi}_{\mathrm{lp},N}^{\mathrm{fp}\ \top}\right] \left[q_{\mathrm{lp},1} \quad q_{\mathrm{lp},2} \quad \cdots \quad q_{\mathrm{lp},N}\right]^{\top}, \tag{20}$$

where $\boldsymbol{\Phi}_{\mathrm{fp}}^{0}$ is a matrix comprising of all critical eigenvectors $\boldsymbol{\phi}_{\mathrm{lp},i}^{\mathrm{fp}}$ of a high-fidelity numerical tangential stiffness matrix $\boldsymbol{K}_{\mathrm{T}}^{\mathrm{num}}$ of the structure, partitioned to the degrees of freedom

corresponding to the probes; and $\boldsymbol{q}$ is the targeted mode contribution vector. The number of critical eigenvectors N extracted from a model may be larger than the number of independent probes N_p. Consequently, some columns in $\boldsymbol{\Phi}_\mathrm{fp}^0$ may be linearly dependent. As the effective independence method requires all columns to be independent, a redundancy-reduction procedure is implemented to choose N_p independent columns from $\boldsymbol{\Phi}_\mathrm{fp}^0$ to form $\boldsymbol{\Phi}_\mathrm{fp}$

$$\boldsymbol{\Phi}_\mathrm{fp} = \begin{bmatrix} \boldsymbol{\phi}_1{}^\top & \boldsymbol{\phi}_2{}^\top & \cdots & \boldsymbol{\phi}_{N_\mathrm{p}}{}^\top \end{bmatrix} = \begin{bmatrix} \phi_{11} & \phi_{21} & \cdots & \phi_{N_\mathrm{p}1} \\ \phi_{12} & \phi_{22} & \cdots & \phi_{N_\mathrm{p}2} \\ \vdots & \vdots & \ddots & \vdots \\ \phi_{1N_\mathrm{p}} & \phi_{2N_\mathrm{p}} & \cdots & \phi_{N_\mathrm{p}N_\mathrm{p}} \end{bmatrix}, \tag{21}$$

where $\boldsymbol{\phi}_i$ are the critical eigenvectors of $\boldsymbol{K}_\mathrm{T}^\mathrm{num}$ partitioned to the degrees of freedom restrained by the probes. Using $\boldsymbol{\Phi}_\mathrm{fp}$, the Fisher information matrix $\boldsymbol{Q}$ can be formed

$$\boldsymbol{Q} = \left(\frac{\partial \Delta \boldsymbol{u}_\mathrm{p}^\mathrm{lp}}{\partial \boldsymbol{q}} \right)^\top \left(\frac{\partial \Delta \boldsymbol{u}_\mathrm{p}^\mathrm{lp}}{\partial \boldsymbol{q}} \right) = \boldsymbol{\Phi}_\mathrm{fp}^\top \boldsymbol{\Phi}_\mathrm{fp}. \tag{22}$$

The determinant of $\boldsymbol{Q}$ corresponds to the *effective independent index* of the probe layout scheme. The scheme with the largest effective independent index corresponds to the layout where probes are located at, or nearest to, the apexes of the critical eigenvectors.

Currently, there is no facility implemented in the Riks solver of ABAQUS to pinpoint critical points and obtain the corresponding critical eigenvectors. Therefore, we adopted an in-house FE code [2] to conduct numerical path-following on the shallow arch to pinpoint all critical points (limit points) on the symmetric-deformation equilibrium path. In this manner, the eigenvectors corresponding to all limit points of $\boldsymbol{K}_\mathrm{T}^\mathrm{num}$ along the equilibrium path can be determined. Based on the critical eigenvector at the first displacement limit point, the effective independence index for the shallow arch with different probe locations is determined, as shown in Fig. 8. The probe location $L_\mathrm{p}/L = 1/4$, which corresponds to the apex of the first limit point eigenvector, has the greatest effective independence index.

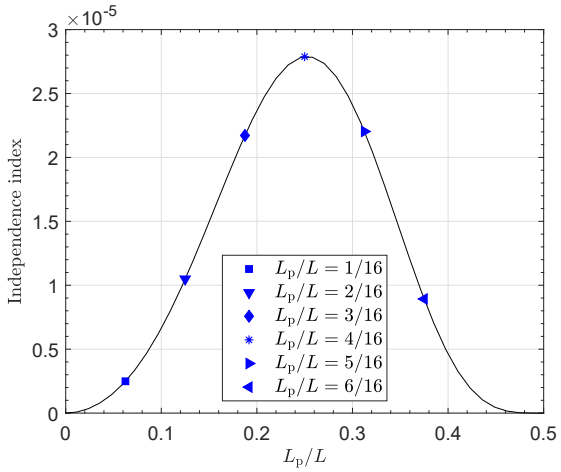

Figure 8: The effective independence index for the arch with different probe locations as shown in Fig. 4b.

One drawback of the effective independence method is that it only accounts for the incremental deformation in close proximity to the limit points; see Eq. (20). We must also consider the factors discussed in previous sections in determining an optimal probe layout. Moreover, the experimental tangent stiffness matrix $\boldsymbol{K}_{\mathrm{T}}^{\mathrm{pp}}$ should be well-conditioned at non-critical equilibria, as any ill-conditioning leads to convergence problems. Generally speaking, the effective independence method provides a good starting point for determining a good probe layout. However, additional parametric studies by means of virtual testing are essential to optimise this layout. Overall, the probe location scheme with $L_{\mathrm{p}}/L = 1/4$ is suggested as the the best trade-off between the different requirements.

4. Tailoring the Control Algorithm to the Experimental Test Case

The virtual testing environment outlined in the previous section can provide recommendations for the optimal probe layout, maximum displacement increments and perturbation sizes. However, in practice experiments are affected by more factors than can be feasibly simulated in a virtual testing environment, *e.g.* the control capability of the actuators, material creeping, friction and slip at connections, manufacturing errors, *etc.* Moreover, the

restart functionality, which works well in a numerical setting to restart the algorithm after a failed convergence attempt, is difficult to implement in an experimental setting due to hysteresis in the test setup. Hence, in this section, an outline of practical refinements to the control algorithms presented previously in Section 2 are introduced, based on experimental observations made during preliminary testing:

1. It is convenient to perturb probe points only (rather than probes *and* main actuation points, as suggested by Eq. (8)) to approximate the tangential stiffness matrix $\boldsymbol{K}_{\mathrm{T}}^{\mathbf{p}}$. This allows $K_{\mathrm{T}}^{\mathrm{pa}}$ to be computed from $K_{\mathrm{T}}^{\mathrm{pa}}$ based on the symmetry of the tangent stiffness matrix. This expedience reduces the time required for the experiment by one-third.
2. The tangent stiffness matrix should be approximated using linear least-squares fitting from the perturbation history (rather than using the initial and final perturbed states via a finite difference approach, as suggested by Eq. (8)). This can relax the requirement for a small perturbation displacement (to ensure linearity), thus reducing the relative effect of experimental noise.
3. The perturbation size is increased in proximity of limit points and a control logic is introduced to approximate the tangential stiffness matrix accurately when there is a kink in the perturbation curve (R_{p} *vs* u_{p}). Note that the kink occurs due to the ability of the arch to break left-right symmetry (a bifurcated path). A small perturbation size or approximation without a control logic would lead to an inaccurate approximation of the tangential stiffness matrix and thus cause convergence problems.
4. Instead of setting $\beta = 0$ as in the numerical setting, an adaptive scheme for varying β in the arc-length equation Eq. (14) is adopted to solve the convergence problem arising from the singularity of $K_{\mathrm{T}}^{\mathrm{pa}}$ and $K_{\mathrm{T}}^{\mathrm{pp}}$. Specifically, when $K_{\mathrm{T}}^{\mathrm{pa}}$ is close to singular, β is set to a large value (we adopt 100 here) and the corrector is achieved by moving the probe points only; when $K_{\mathrm{T}}^{\mathrm{pp}}$ is close to singular, β is set to zero and the corrector is

achieved by moving the main actuation point only.

5. An upper limit on the incremental displacement at the control points is set to prevent the control points from overshooting beyond limit points as well as prevent the arch specimen from physically breaking.
6. The predictor displacement at the probes is determined purely from the 'tangential' component arising from the applied displacements at the actuation point, u_{a}, in the regions where the arch deviates from the actual equilibrium after perturbation due to hysteresis and friction at connections. This effectively prevents potential convergence problems caused by the reaction force at the probes exceeding the tolerance after the perturbation step.
7. The predictor direction reversal at limit points is determined based on the sign change in $K_{\mathrm{T}}^{\mathrm{pp}}$ only. In the current one-probe system, the sign change in either $K_{\mathrm{T}}^{\mathrm{pa}}$ or $K_{\mathrm{T}}^{\mathrm{pp}}$ leads to this sign change in direction, referring to Eq. (17). However, only the sign change in $K_{\mathrm{T}}^{\mathrm{pp}}$ corresponds to a traversal of a limit point in the actuation point displacement.

A detailed exposition of these refinements can be found in Appendix B. These modifications highlight the importance of fine-tuning the experimental path-following algorithm to specific applications, much like numerical path-following algorithms must be fine-tuned for individual simulations to efficiently achieve desired results.

5. Experimental Setup and Results

Having established an algorithmic framework as well as a virtual testing environment for experimental path-following, a symmetric shallow arch is tested using one pair of coupled probes (to enforce symmetry). Even though this is a restriction in terms of the possible equilibria that can be observed, it does not change the qualitative nature of the equilibria that are indeed observed; namely, both stable and unstable equilibria, as well as limit points.

5.1. Experimental Setup

The geometric and material properties of the arch are as presented in Section 3. Test pieces were laser cut from sheets of arcylic; the mechanical properties were found from coupon test results [22] with a Young's modulus and Poisson's ratio of $E = 3200\,\text{MPa}$ and $\nu = 0.38$, respectively. The nominal dimensions of the specimens are $L = 205\,\text{mm}$, $h = 20\,\text{mm}$, $t = 1.57\,\text{mm}$ as per Fig. 4, and depth $D = 4.68\,\text{mm}$. The test setup is shown in Fig. 9. To connect the probes and the supports via pinned connections, loops are incorporated during laser cutting; see Fig. 9d and f. Arches with probe locations at $L_\text{p} = L/6$, $L/4$ and $L/3$ were manufactured and tested to confirm the optimal probe location ($L_\text{p} = L/4$) established during virtual testing.

Two independent displacement-controlled inputs—one for the main actuation point at the mid-span and one for the probes—are used. A purpose-built experimental setup was used to (i) provide pinned support to the arch at its edges, (ii) control the position of the main actuation point, and (iii) measure the main actuation point reaction force. Specifically, an SKF CARE 33 linear actuator, a Gefran PZ34-A-250 linear transducer and a $\pm 250\,\text{N}$ load cell manufactured by Applied Measurement Ltd were used for the main actuation point. The custom frame was fixed to the base of an Instron 8872 hydraulic test machine, which was used to control the probe positions. An Instron Dynacell $\pm 250\,\text{N}$ dynamic load cell was used to measure the reaction forces at the probes, *i.e.* the sum of the reaction forces at the two linked, symmetrically placed probes.

The overall change of the probe reaction force throughout the loading cycle is close to zero (the target for equilibria is $R_\text{p} = 0$), making the measurement sensitive to noise and data drift of the load cell. Based on the manufacturer's calibration report of the load cell and preliminary testing, a mass with a weight of $20\,\text{N}$ was added to the load cell as dead load. With this pre-loading, the error in the measurement is smaller than $0.01\,\text{N}$ and the effects of data drift are minimised.

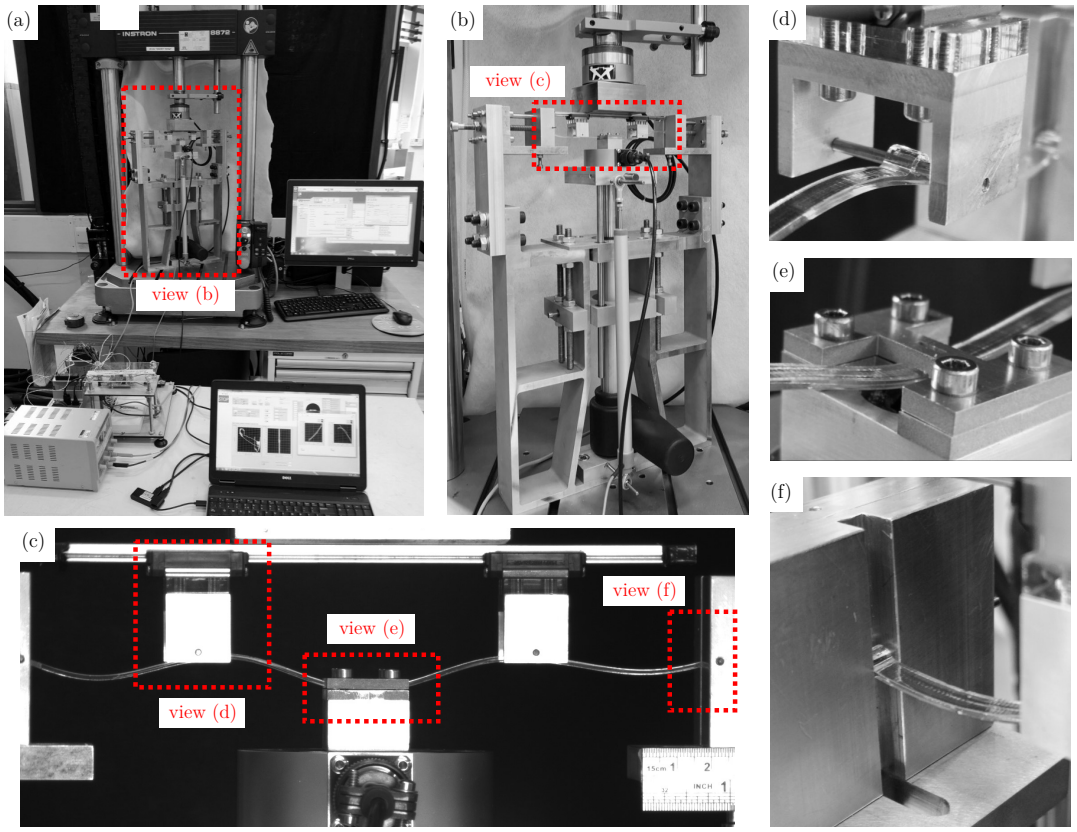

Figure 9: Experimental setup: (a) LabVIEW laptop and electronics in front of the Instron universial testing machine; (b) the test frame with linear transducer, actuator and load cell attached to the base of the Instron; (c) the deformed arch specimen with central actuation point and probes attached; (d) the pins that attach the probes to the arch; (e) the I-shaped plates clamping the arch midpoint to enforce symmetry; (f) the end of the arch pinned at a support block.

The probes were attached to the arch using 2 mm diameter pins through loops in the arch, as shown in Fig. 9d. The pins were designed to be as noninvasive as possible and were lubricated to reduce the effects of friction. The probes were mounted on a linear rail (also lubricated) to allow movement in the horizontal direction, while enforcing the same vertical displacement. The midpoint of the arch (the actuation point) was clamped between two plates (an I-shaped clamp) to prevent rotation, and thus enforce symmetry. The width of the clamp area was 5 mm and two orthogonal rectangular slots ensured that the actuation point is strictly located at the arch mid-span. The pinned end boundary conditions were

implemented using 2 mm diameter steel pins through built-in loops on the arch and support blocks, as shown in Fig. 9f. Compared with the wedged ends used in previous work [22], the effects of slip and friction are smaller for the pinned configuration used here.

LabVIEW (version 14.0) was used to measure the reaction forces and control the displacements of the main actuation point and the probes. The path-following algorithm and supporting computations were also implemented in LabVIEW, and can be found as supplementary material on the data repository of the University of Bristol [34]. In the controlling algorithm, the perturbation size to determine the experimental tangent stiffness matrix is set to 0.5 mm and 1.2 mm on stable and unstable equilibrium branches, respectively. The incremental displacement at the controlling points is limited to 0.2 mm when $\boldsymbol{K}_{\mathrm{T}}^{\mathrm{pa}}$ falls below a tolerance of 1.0 N/mm, and limited to 0.5 mm when $\boldsymbol{K}_{\mathrm{T}}^{\mathrm{pp}}$ falls below the same tolerance. The total residual reaction force tolerance at the probes for equilibrium convergence is 0.2 N for the arch with probes at $L_{\mathrm{p}} = L/6$ and 0.1 N for the other two cases ($L_{\mathrm{p}} = L/4$ and $L_{\mathrm{p}} = L/3$). The predictor displacement at the main actuation point in the first step is 0.5 mm. The desired number of iterations for convergence of each loading step is 3 (used to automatically control the step size using Eq. (16)).

5.2. Experimental Procedure and Results

For each arch, the experiment was performed in two stages. In the first stage, the test was performed with displacement control at the main actuation point only (no probes), as indicated by the black curves in Figs. 10–12a. The actuation point displacement u_{a} was increased until the fully inverted arch shape was obtained. Only the stable portion of the equilibrium path, up to the first displacement limit point L_1, can be traced in this manner because at limit point L_1 the arch snaps down into the inverted configuration. Following snap-through, u_{a} was decreased to revert the arch back into the original unloaded position. Upon decreasing displacement, the arch snaps back into the original configuration at limit point L_2. Thus, under the midpoint, displacement-controlled loading, the arch undergoes

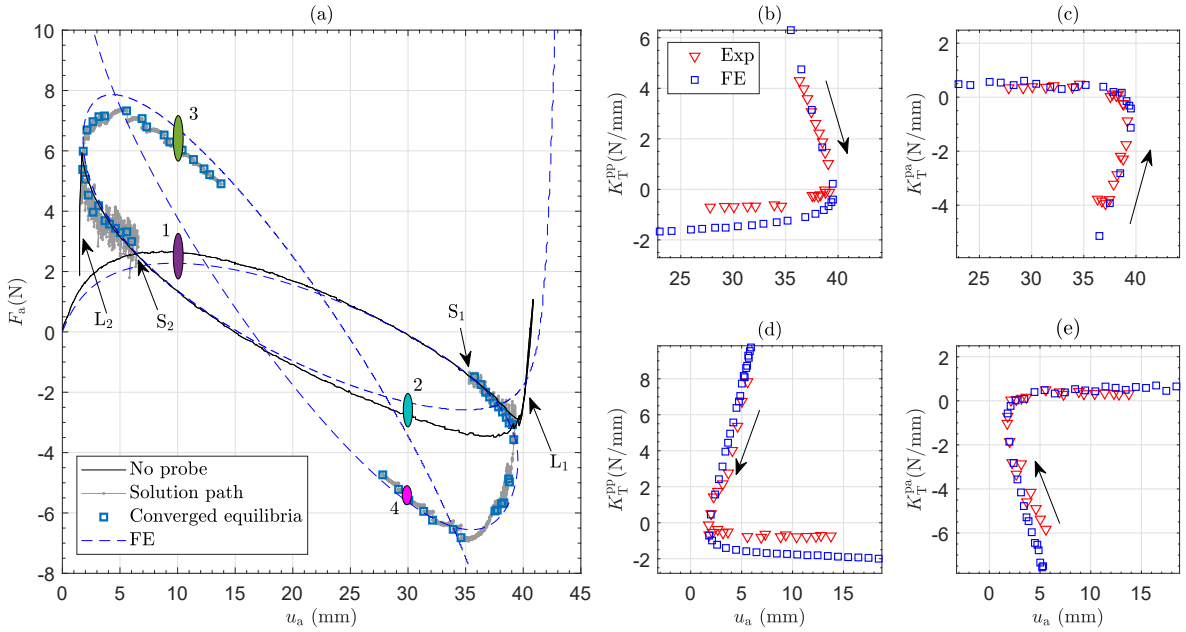

Figure 10: Experimental path-following results for the arch with linked probes at $L_p = L/6$. (a) Comparison of the load-displacement equilibrium plots obtained by experimental path-following and a quasi-static Riks solver in the FEM software ABAQUS. (b–e) Comparison of the tangent stiffness matrix components along the equilibrium path obtained from experimental testing and the virtual testing environment; (b–c) starting from S_1 and (d–e) starting from S_2. Arrows denote the loading direction.

snap-through at the two displacement limit points in u_a, L_1 and L_2. In the second stage, the arch was loaded to a position just before the limit point (S_1 and S_2 in Fig. 10–12) using displacement-controlled loading at the mid-span. The probes were then attached to the arch, and the path-following algorithm initiated. The experiment was performed from both starting points S_1 and S_2 in order to traverse both L_1 (from S_1) and L_2 (from S_2). The path-following algorithm was manually stopped after the limit point had been traversed.

Figures 10–12 present the results from the experimental path-following tests for the three different probe locations, $L_p = L/6$, $L/4$ and $L/3$, respectively. The grey dotted lines and blue hollow squares represent the predictor-corrector solution process and all converged equilibria, respectively. In all three arch cases, limit points in u_a are successfully traversed and the unstable path beyond the the limit point is traced. For verification, results obtained

using the quasi-static Riks solver implemented in ABAQUS are presented by dashed lines. The experimental results generally show good correlation with the FE benchmark. The results are encouraging given the strong sensitivity to imperfections of nonlinear systems.

The main sources of experimental error and uncertainty stem from: (i) creep/relaxation of the acrylic material during testing; (ii) geometric irregularities introduced from the laser cutter during manufacturing of the specimens; (iii) drifting effects in the force measurement system; (iv) local stiffening effects of the loops introduced to attach the probes; and (v) friction and slip at, especially, the probe connections. These effects are discussed in more detail in Section 6.1.

Panels b–e in Figs. 10–12 show the tangent stiffness components $K_{\mathrm{T}}^{\mathrm{pp}}$ and $K_{\mathrm{T}}^{\mathrm{pa}}$ computed during the experiment at each converged equilibrium. Superimposed as blue hollow squares are the results from virtual testing. Good correlation is demonstrated throughout. This in turn validates the predictive capability and benefit of using the virtual testing environment as a surrogate experiment.

Figure 13 presents the deformed shapes of the tested arch and the corresponding results from the FE simulation. Arch shapes observed on the two unstable portions of the equilibrium path (points 3 and 4) match those from the FE simulation, both in terms of the number and position of half-waves. For probe locations at $L_{\mathrm{p}} = L/3$, the arch shape at point 4 was not accessible as the arch snapped through near the limit point. From the arch deformation shapes at stable equilibria (points 1 and 2), the tested arches deform less than the FE model due to the fact that the loops created to connect the probes act as local stiffeners.

Overall, by comparing the equilibrium paths and tangent stiffness quantities for the three different probe locations presented in Figs. 10–12, probe location $L_{\mathrm{p}} = L/4$ results in the closest correlation with the FE benchmark for the equilibrium path and with the virtual testing results for the tangent stiffness components. This confirms the preliminary conclusion

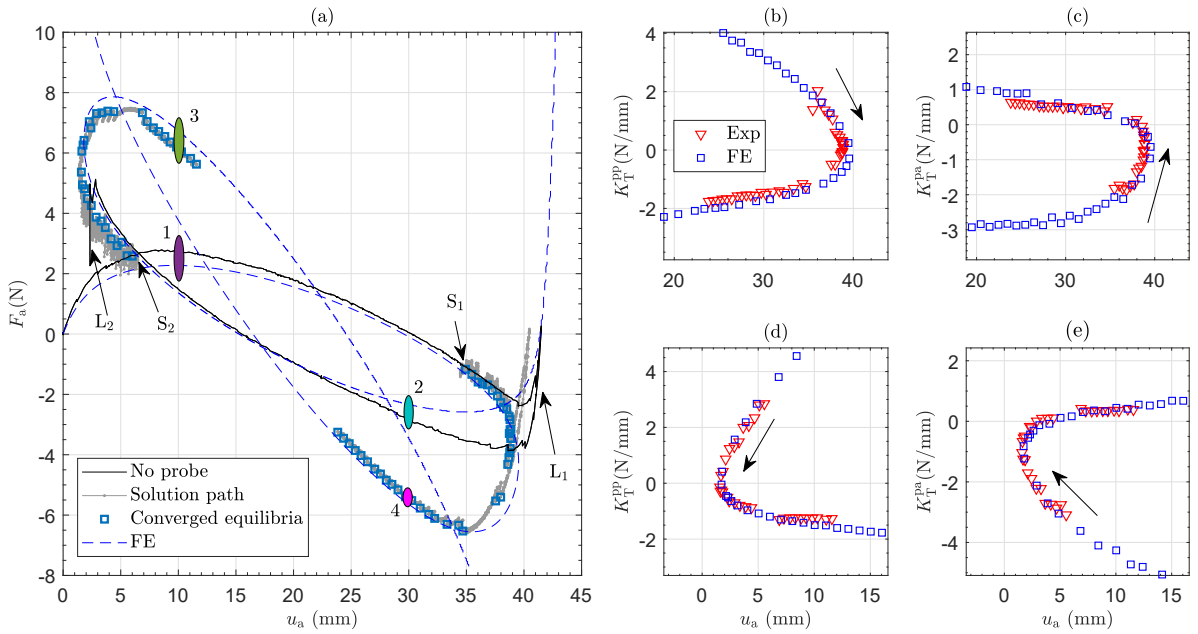

Figure 11: Experimental path-following results for the arch with probe locations at $L_p = L/4$. Subfigures (a–e) are as described in Fig. 10.

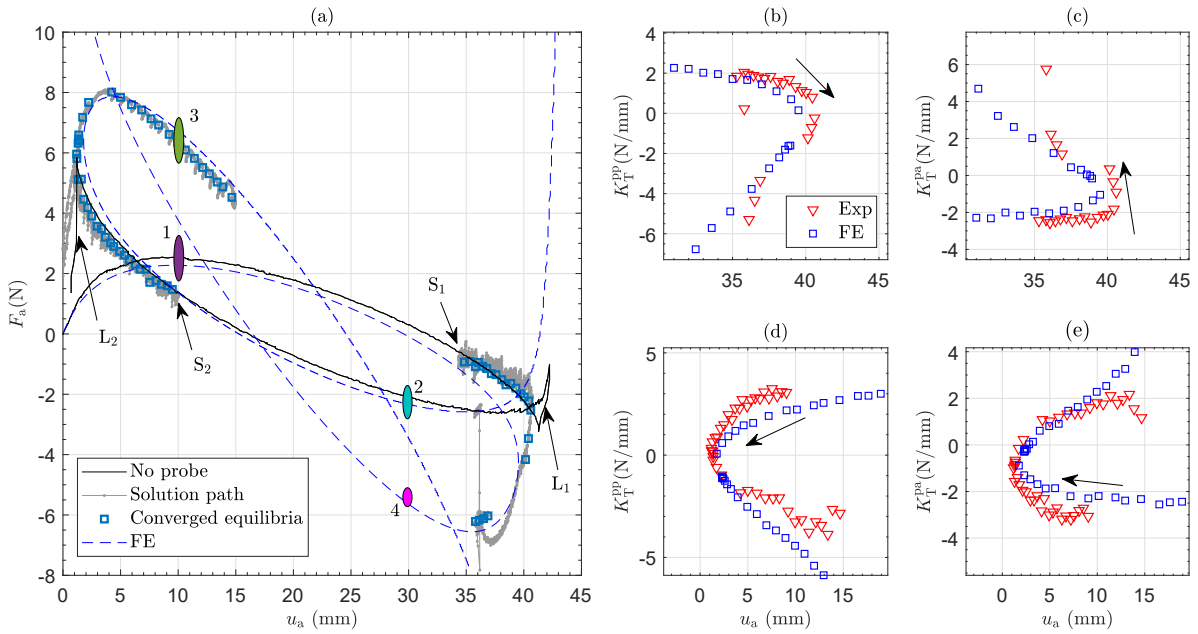

Figure 12: Experimental path-following results for the arch with probe location $L_p = L/3$. Subfigures (a–e) are as described in Fig. 10.

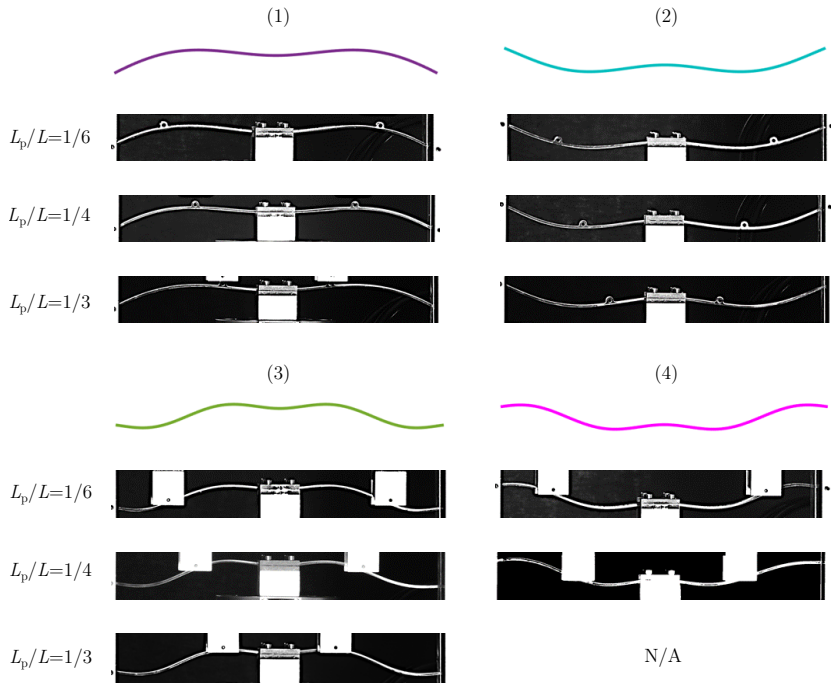

Figure 13: Arch deformation shapes from the FE model and the experimental results at points 1–4 (defined in Figs. 10–12) for different probe locations. For the case of $L_p = L/3$, the arch shape at point 4 is inaccessible due to snap-through near the limit point, as shown in Fig. 12.

reported from virtual testing and effective independence index method that $L_p = L/4$ can be considered as the best probe location for controlling the arch.

Figure 14 details the measurements near limit point L_2 for the arch with probes at $L_p = L/4$. Generally, the magnitude of the residual probe force at converged equilibria is smaller than the prescribed convergence tolerance $R_{p,tol} = 0.1\,N$. This means that the experimental test setup would have supported a tighter convergence tolerance. However, as previously established through virtual testing, accurate results can nonetheless be achieved with greater values of the convergence tolerance with the benefit of shorter experimentation time. To conclude, we note that the experimental results correlate better with the numerical benchmark equilibrium curve than the previous experimental results of the 'step-scan' method [22].

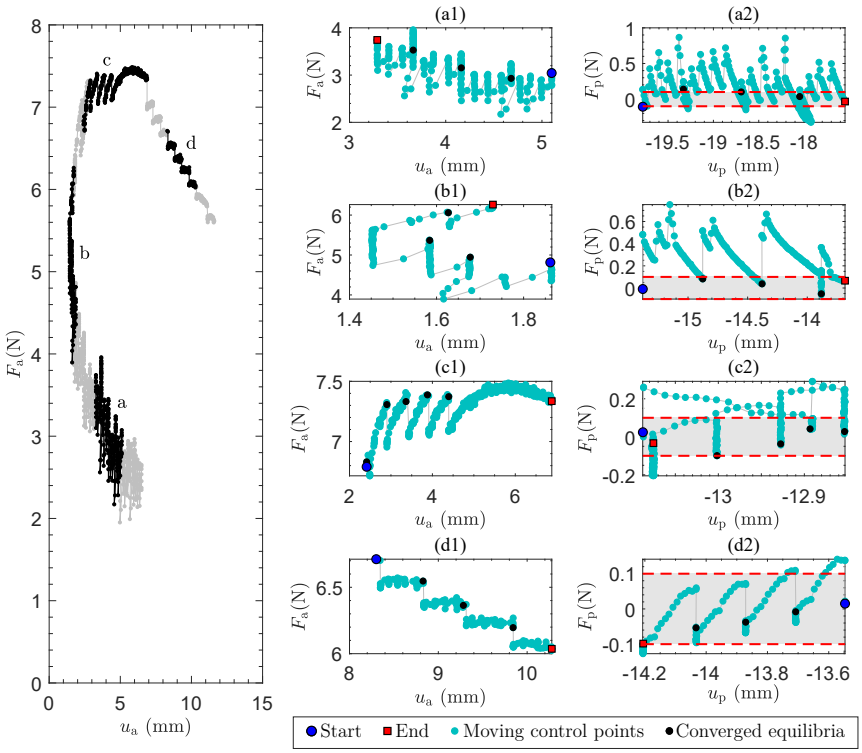

Figure 14: Details of experimental path-following results near limit point L_2 for the arch with probe locations at $L_p = L/4$. Segments of interest are highlighted: segments (a) and (b) are stable, while (c) and (d) are unstable segments of the equilibrium path. The subplots on the right show detailed views of the data in each area of interest. The middle column of subplots (a1–d1) are zoomed-in views of the equilibrium curve (u_a *vs* F_a space). The right column of subplots (a2–d2) show the F_p *vs* u_p data collected from the probes. The colours on subplots (a1—d2) indicate different algorithm states: black dots are converged equilibria, cyan dots represent the predictor-corrector process. The dashed red lines indicate the converged equilibrium tolerance $|F_p| < 0.1\,\mathrm{N}$. The blue dot and red square indicate, respectively, the first and last data point logged in the area of interest during the testing sequence.

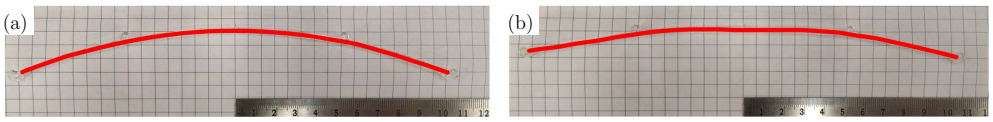

Figure 15: Arch geometry (a) before and (b) immediately after a test. The probe location is $L_\mathrm{p} = L/4$ and residual deformations between the probe points are clearly visible.

6. Discussion

The good correlation between experimental path-following measurements and FE simulations for the three different probe locations demonstrates the general robustness of the proposed path-following algorithm. In this section, different sources for discrepancies between the experimental results and FE predictions are discussed. Next, the cause of 'spikes' and large corrector increments in proximity of limit points in u_a is analysed, and the sensitivity to probe locations is evaluated. Lastly, we comment on the application of the current work to the design of future experiments.

6.1. Sources of Experimental Error

The discrepancy between the experiments and numerical predictions is primarily attributed to creep in the acrylic arches, which is induced by the high strains imposed along the unstable segments of the equilibrium path, where the arch is deformed into higher-order modes (FE simulations for $L_\mathrm{p} = L/4$ show maximum strains of 2.25e-2 after traversal of the limit point). This conclusion is supported by the fact that, after testing, the specimens did not immediately return to their original stress-free shape upon detachment of the probes, as shown in Fig. 15. The acrylic material was selected for convenience of manufacture, rather than for its mechanical properties.

Additional sources of experimental error stem from geometric imperfections introduced during the manufacturing process. The arches are cut from sheets of acrylic using a laser cutter. The heat produced expands the acrylic sheet non-uniformly, resulting in a variable

arch shape. Measured geometric variables were used in the FE models, but local thickness variation or details such as local stiffening at the probe points were not captured.

A further source of experimental error is sensor drifting in the force measurement system. The measurement range of the load cell connected to the probes is ±250 N. However, during experimental path-following, the reaction force range at the probes is only within approximately ±4 N. Even though the load cell was zeroed before the test and a preload of 20 N was placed on the load cell, the force reading at the linked probes did not return exactly to zero when the arch was detached from the probes after the test.

Finally, hysteresis due to friction and slip at the connections also contributes to discrepancies between theory and experiments. The connection loops on the arch are manufactured to be as noninvasive as possible, and lubricant was sprayed on all connections. Nonetheless, it was observed that the arch did not return to the original equilibrium state after the perturbation process to compute the tangent stiffness matrix. Specifically, the reaction forces at the probe points were not the same before and after perturbation, especially in the proximity of the limit points in u_{a} and u_{p}.

6.2. Predictor-Corrector 'Spikes' and Large Corrector Increments

The 'spikes' observed on the solution paths near limit points L_1 in Fig. 11 and L_2 in Fig. 12 are caused by an incorrect determination of the sign of $K_{\mathrm{T}}^{\mathrm{pa}}$. The monitoring functionality presented in Appendix C is able to detect and correct this error automatically.

Beyond limit points, there is a relatively large corrector step, corresponding to the region where $K_{\mathrm{T}}^{\mathrm{pa}}$ changes sign; see Fig. 11c,e. Consider, for example, the result of the arch with probe location at $L_{\mathrm{p}} = L/4$ loaded from point S_1 onward. Figure 16a presents a perturbation cycle to compute $\boldsymbol{K}_{\mathrm{T}}^{\mathrm{ap}}$ for an equilibrium state just before a large corrector increment. Due to material hysteresis and friction at connections, the loading path (adding a perturbation) is different from the unloading path (removing the perturbation). Figure 16b presents the relationship between the residual reaction force at the probes R_{p} and the displacement at

the main actuation point u_{a}, during the large corrector increments. Initially, the first two corrector increments are ineffective and the reaction force actually increases, which implies that the computed $K_{\mathrm{T}}^{\mathrm{pa}}$ is of the wrong sign. As the actuation point moves further, R_{p} decreases, implying that the computed $K_{\mathrm{T}}^{\mathrm{pa}}$ is now of the the correct sign. The initial ineffective corrector and the small magnitude of $K_{\mathrm{T}}^{\mathrm{pa}}$ lead to large corrector increments (so-called 'spikes').

One solution to this problem is to impose a less stringent tolerance for convergence so that convergence can be reached after the predictor step. However, a less stringent tolerance naturally leads to less accurate results and can cause the control algorithm to converge to a different equilibrium branch. Another solution is to force corrective iterations to be made by moving only the probes. However, as noted in Section 4, the residual reaction forces at the probes after perturbation cause u_{p} to deviate from the actual equilibrium. Under these circumstances the corrector process is also inefficient due to the initial positive stiffness in the R_{p} *vs* u_{p} relationship. In conclusion, there appears to be no ideal solution for the problem due to the property of the structure that the configurations for the sign change of $K_{\mathrm{T}}^{\mathrm{pa}}$ and $K_{\mathrm{T}}^{\mathrm{pp}}$ are very close.

6.3. Probe Location Sensitivity

The experimental results confirm the hypothesis that the probe location $L_{\mathrm{p}} = L/4$ is most effective for traversal of the limit points considered here. When the probes move away from this optimal location, the variation of the tangent stiffness matrix as well as the residual reaction force during the predictor-corrector process increases. When moving the probes closer to the supports ($L_{\mathrm{p}} = L/6$), the effect of friction is larger, explaining the larger probe residual reaction force tolerance ($R_{\mathrm{p,tol}} = 0.2\,\mathrm{N}$ for $L_{\mathrm{p}} = L/6$ and $R_{\mathrm{p,tol}} = 0.1\,\mathrm{N}$ for $L_{\mathrm{p}} = L/4$ and $L_{\mathrm{p}} = L/3$). Alternatively, when the probes move towards the mid-span ($L_{\mathrm{p}} = L/3$), they lose 'control authority' over the arch such that the unsupported sections snap-through dynamically. As shown in Fig. 12a, as the arch with $L_{\mathrm{p}} = L/3$ is loaded from point S_1,

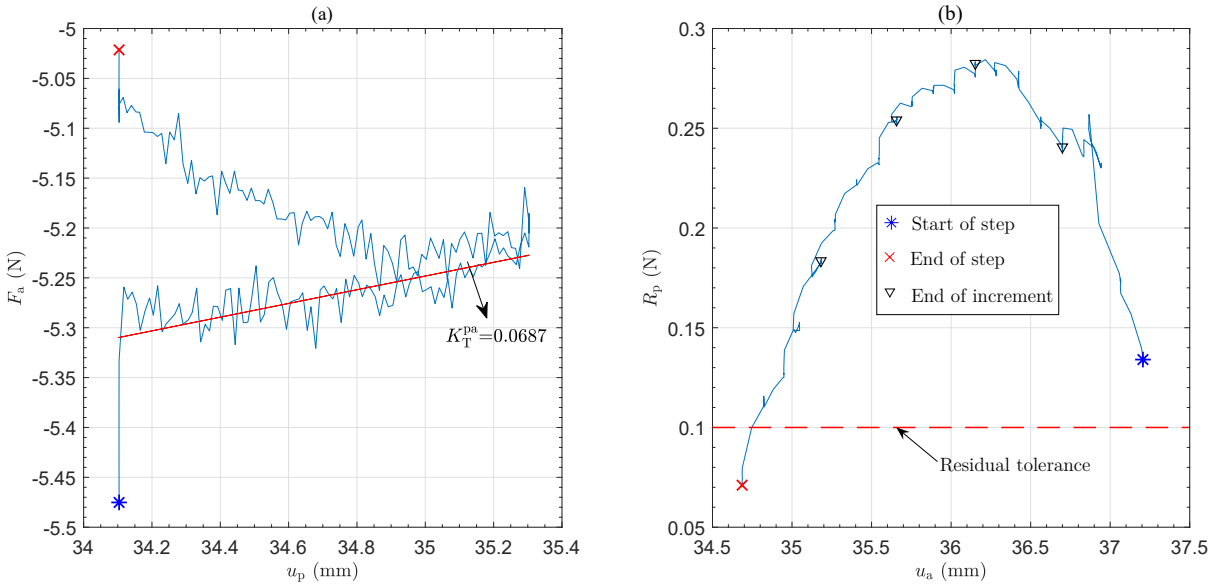

Figure 16: (a) Reaction force at the main actuation point *vs* the displacement at the probes during the perturbation process to obtain the tangent stiffness matrix. The converged equilibrium state corresponds to a state just before a large corrector increment as shown in Fig. 11 (probe location is $L_p = L/4$ and loading is from point S_1 onward). The red line represents the fitted linear curve based on least squares to approximate K_T^{pa}. Stars and crosses represent the start and end of the loading process. (b) The residual reaction force at the probes versus the displacement at the main actuation point during the corrector increments. Triangles represent the end of each increment. The dashed line represents the tolerance for convergence.

the path-following process fails to converge on the original equilibrium path and jumps to another branch immediately after traversing the limit point. In this case, the last converged equilibrium state is in the proximity of the limit point of u_p, corresponding to a change in sign in K_T^{pa}. The limit point in u_p is traversed during the perturbation process and the unrestrained portions of the arch between the probe and the supports snap-through, as shown in Fig. 17. Once the perturbation is reversed, the arch does not return exactly to its previous equilibrium state, even though the probes themselves return to their original position. In other words, the probes lose control authority over the arch and additional probes are required to stabilise the unsupported portions of the arch.

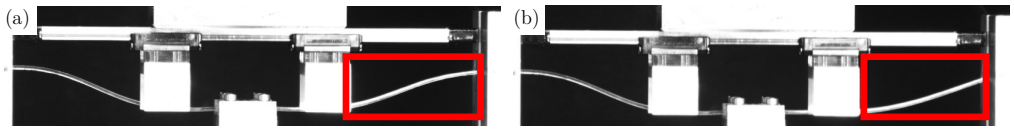

Figure 17: Arch mode shapes (a) before and (b) after snap-through during the perturbation process to obtain the experimental tangent stiffness matrix for the arch with probe location $L_p = L/3$ and loading from point S_1 onward. The red box indicates where snap-through occurs. The snap-through process corresponds to the vertical grey line in Fig. 12a.

6.4. Implementation in Future Experiments

The control algorithms outlined in Section 2.2 provide a general methodology for experimental path-following of nonlinear structures, which is independent of the underlying structure, the number of probing points or their specific implementation (*e.g.* a rotational input). The adjustments and refinements to the algorithm, presented in Section 4, to reduce the impact of noise and measurement uncertainty were informed by the particular test case and experimental implementation described in this work. Nonetheless, the algorithm maintains the general predictor-corrector scheme of Newton's method, and many lessons learned will be applicable to future experiments on different structures that exhibit limit point instabilities. It is important to emphasise that any experimental path-following implementation will need to be tailored to the specific application, including fine-tuning of the algorithm parameters to handle the effects of sensor noise and uncertain boundary conditions (*i.e.* friction, slack). This is analogous to selecting appropriate parameters for numerical path-following in finite element simulations of the same structures. The details outlined herein will therefore provide guidance for the set-up of future experiments.

7. Conclusions

We have presented a new experimental testing method for nonlinear structures that mimics the path-following capability provided in commercial FE codes. In addition to loading the structure via the main actuation points, additional actuators and sensors are attached at

so-called 'probe points'. The purpose of the probe points is to control the overall shape of the structure and stabilise otherwise unstable equilibria [22]. Furthermore, the probes are used to compute an experimental tangent stiffness matrix. Access to this structural quantity enables the use of well-established algorithms based on Newton's method to successively step away from a known equilibrium and iteratively converge to a new equilibrium state. Using this feedback control system, we guide the structure along an equilibrium path such that both stable and unstable equilibria can be path-followed, and limit points in the forcing parameter traversed. The robustness of the control algorithm has been demonstrated by applying the experimental path-following method to a transversely loaded shallow arch.

The experimental path-following method introduces increased complexity compared to a conventional testing set up (additional actuators, sensors and control algorithms). Virtual testing of the experiment via a computational surrogate proved crucial to determine the optimal testing parameters. Another advantage of the presented virtual testing environment is that additional features, such as increasing the number of control points on the structure, can quickly be demonstrated in principle.

The developed experimental path-following methods enhance testing capabilities of multi-functional structures, such as shape-adaptive structures, and could lead to a certification platform that builds confidence in the safe operation of novel nonlinear or post-buckled structures. At the same time, experimental path-following can be used as a tool to interrogate, through an experimental tangent stiffness matrix, the stability of structure under test, and thereby lead to a non-destructive testing method for imperfection-sensitive thin-walled constructions.

In Part II of this paper, we use the virtual testing environment to demonstrate that more complex features typical of numerical path-following techniques can be replicated in an experimental setting based on the fundamental building block of shape control and the computation of an experimental tangent stiffness matrix. These advanced concepts include—

but are not limited to—pinpointing of critical points, branch switching at symmetry-breaking bifurcations, and tracing of critical points with respect to additional parameters.

Acknowledgments

R.M.J.G. is funded by the Royal Academy of Engineering under the Research Fellowship scheme [Grant No. RF\201718\17178]. J.S. and A.P. are funded by the UK Engineering and Physical Sciences Research Council [Grant No. EP/M013170/1].

Data Statement

Data are available at the University of Bristol data repository, data.bris, at `https://doi.org/10.5523/bris.932lqv3akioz2jrwngdxzshfo`.

Appendix A. Control Algorithm

The procedure of the predictor-corrector scheme to implement experimental path-following is also summarised in Fig. Appendix A.1. The algorithm is followed for each load step, where a load step is defined as the movement from a known equilibrium configuration to another along the equilibrium manifold.

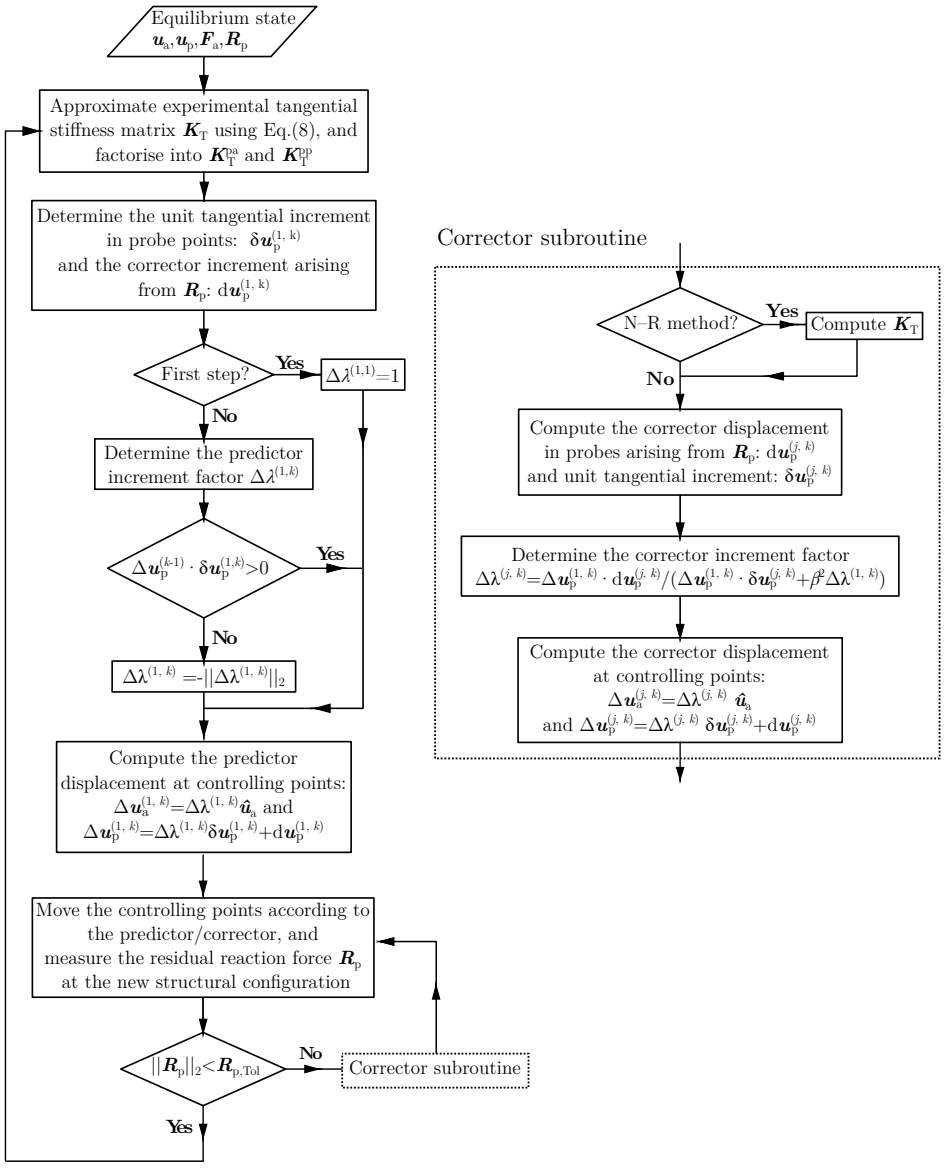

Figure Appendix A.1: Procedure for experimental path-following of equilibria.

Appendix B. Tailoring the Control Algorithm to the Experimental Test Case

Appendix B.1. Minimising Perturbations

Following Eq. (8), all control points (main actuation and probe points) are perturbed in turn to obtain the tangent stiffness matrix components ($\boldsymbol{K}_{\mathrm{T}}^{\mathrm{p}} = [K_{\mathrm{T}}^{\mathrm{pp}}\ K_{\mathrm{T}}^{\mathrm{pa}}]$ for the shallow arch with one actuation point and one probe pair) via finite differences of the probe reaction forces. The perturbation process to determine $\boldsymbol{K}_{\mathrm{T}}^{\mathrm{p}}$ is by far the most time-consuming process during each load step. The efficiency of the experimental procedure can be improved by nearly one third if the process is restricted to perturbing the probe points only (rather than probes *and* main actuation points). Due to the symmetry of the tangent stiffness matrix, the terms $K_{\mathrm{T}}^{\mathrm{pa}}$ and $K_{\mathrm{T}}^{\mathrm{ap}}$ should be identical. Hence, using the property that $K_{\mathrm{T}}^{\mathrm{pa}} = K_{\mathrm{T}}^{\mathrm{ap}}$, we compute $K_{\mathrm{T}}^{\mathrm{pa}}$ by perturbing the probes and measuring the change in reaction force at the main actuation point (rather than moving the main actuation point and measuring the change in reaction force at the probes).

Preliminary testing showed that $K_{\mathrm{T}}^{\mathrm{pa}}$ and $K_{\mathrm{T}}^{\mathrm{ap}}$ are indeed very close as long as the perturbation displacement remains reasonably small. Differences between the two components only become significant when $K_{\mathrm{T}}^{\mathrm{ap}}$ is close to zero, corresponding to a state where u_{p} reaches a limit point. In this case, moving the probes can suddenly change the arch's shape during perturbation. When most of the displacement during the corrective steps relies on moving the actuation point, an inaccurate approximation of $K_{\mathrm{T}}^{\mathrm{ap}}$ slows down convergence or even causes divergence. A subroutine to modify $K_{\mathrm{T}}^{\mathrm{ap}}$ in these circumstances is described in detail in Appendix C.

Appendix B.2. Varying Perturbation Magnitude

Recalling Eq. (8), only the reaction forces at the initial and final perturbed states are needed to approximate the tangent stiffness matrix via finite differences. In reality, a number of difficulties arise with this simple two-point linear computation. Virtual testing on the tested arch revealed that: (i) $\boldsymbol{K}_{\mathrm{T}}^{\mathrm{p}}$ obtained using the finite difference approximation based on two

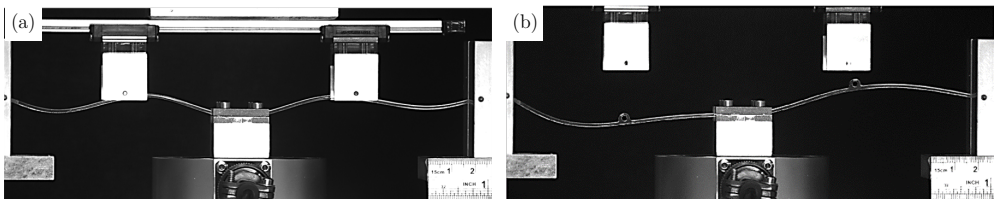

Figure Appendix B.1: The deformed arch configuration (a) before and (b) after detaching the probes on the unstable path. Note that the arch was loaded from the inverted configuration. The left part snaps back to the initial loading shape and the right part snaps through.

data points is sensitive to noise; and (ii) the reaction force-perturbation displacement (R_p *vs* u_p) relationship is generally linear for all equilibria up to a perturbation size of 1.5 mm, except for states that are in the proximity of limit points in u_p. Further, it was found that 'slack' in the experimental setup complicates the finite difference approximation of the experimental tangent stiffness matrix. For example, stick-slip at pinned connections, at probe–arch and support boundaries, results in a nonlinear initial portion of the R_p *vs* u_p response. To overcome these issues, a linear least-squares fitting approach is adopted to approximate the tangent stiffness matrix from the perturbation history. The number of data points used for the fitting is related with the perturbation size. Generally, at least thirty data points are adopted. By relying on a least-squares fit, the requirement for a small perturbation displacement (to ensure linearity) is also relaxed, reducing the relative effect of experimental noise in determining the tangent stiffness matrix (as reaction forces at the probes are greater).

Another practical issue in computing the tangent stiffness matrix for the present experiment is a side effect of enforcing left-right symmetry of the arch, using a linked pair of probes. Due to manufacturing and installation imperfections, the arch tested is not inherently symmetric and thus has a natural inclination to break symmetry. On the unstable equilibrium branch it was observed that when the probes are detached, one half of the arch may snap upwards while the other snaps downwards, see Fig. Appendix B.1. This implies

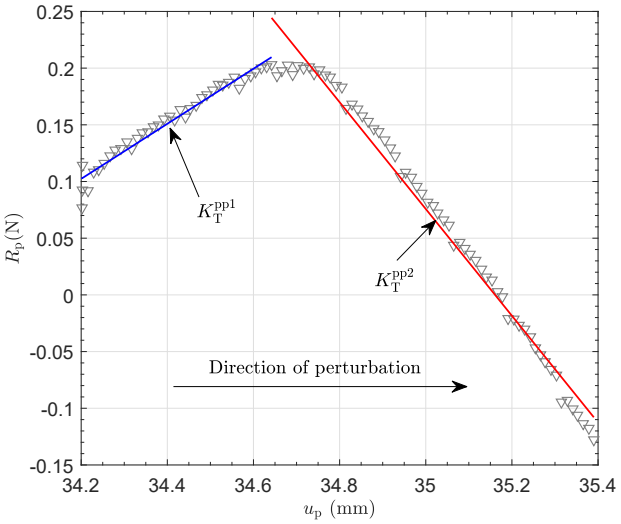

Figure Appendix B.2: The relationship between the residual reaction force and perturbation displacement at the probes during the perturbation process to obtain the tangent stiffness matrix on the unstable equilibrium path. Blue and red lines represent the fitted linear curves based on least squares to approximate K_T^{pp}.

that during the initial probe perturbation process one side of the probe pair perturbs the structure first and the arch is then forced to be symmetric. As a result, the tangent of the R_p *vs* u_p relationship can be initially positive and then change sign as the perturbation size increases (see Fig. Appendix B.2). This is a drawback of the coupled probe scheme: the measured probe reaction force is the summation of the two individual probe forces, but not necessarily double the force at each probe. To better capture the behaviour of the arch, the probes should be decoupled, which requires an additional actuator and force measurement sensor. In addition to increased experimental complexity, this will also expand the size of the tangential stiffness matrix and decrease the experimental efficiency.

Thus, to overcome the problem associated with the inherent asymmetry of the arch, a relatively large perturbation size needs to be adopted when K_T^{pp} falls below a threshold value (implying that the arch is nearing a limit point). Here, we increase the perturbation size from 0.5 mm to 1.2 mm when $K_T^{pp} < 1.0\,\mathrm{N/mm}$. Furthermore, additional control logic is

required to deal with the kink in the R_p *vs* u_p measurements highlighted in Fig. Appendix B.2. Instead of using the whole data set from the R_p *vs* u_p curve to establish a least squares fit of the stiffness, a portion of the data on either side of the kink is used. These two least square fits are denoted by blue and red lines in Fig. Appendix B.2. Because there are two possible tangent stiffness values, $K_\mathrm{T}^{\mathrm{pp1}}$ and $K_\mathrm{T}^{\mathrm{pp2}}$, we establish a criterion to choose between the two values:

$$\begin{aligned}
&\textbf{if } \left(u_\mathrm{p}^{(j,k-1)} + \Delta u_{\mathrm{p,max}}\right) > u_{\mathrm{p,LP}}^{(j,k)} \text{ or } \left(u_{\mathrm{p,LP}}^{(j,k)} - u_{\mathrm{p,eq}}^{(j,k)}\right)/\Delta u_\mathrm{p} < \Gamma \\
&\quad K_\mathrm{T}^{\mathrm{pp}} = K_\mathrm{T}^{\mathrm{pp2}}, \\
&\textbf{else} \\
&\quad K_\mathrm{T}^{\mathrm{pp}} = K_\mathrm{T}^{\mathrm{pp1}},
\end{aligned} \tag{B.1}$$

where $u_\mathrm{p}^{(j,k-1)}$ is the probe displacement of the last converged state; $\Delta u_{\mathrm{p,max}}$ is the maximum displacement increment for the probes; $u_{\mathrm{p,LP}}^{(j,k)}$ is the probe displacement corresponding to the limit point in the R_p *vs* u_p response; Δu_p is the perturbation size; and Γ is the chosen threshold value. If Γ is small, the condition to adopt $K_\mathrm{T}^{\mathrm{pp}} = K_\mathrm{T}^{\mathrm{pp2}}$ is more strict, which can lead to overshooting beyond the kink. If Γ is large, the kink can be predicted prematurely. Here, $\Gamma = 0.4$.

Appendix B.3. Varying Arc-length Equation

As described in Section 2.2, the parameter β defines the nature of how the corrector increment is applied; see Eq. (10). In a numerical path-following environment, it is generally accepted that $\beta = 0$ is a robust choice for most problems [30]. In this case, the arc-length equation can be simplified to

$$\Delta \boldsymbol{u}_\mathrm{p}^{(1,k)} \cdot \Delta \boldsymbol{u}_\mathrm{p}^{(j,k)} = 0. \tag{B.2}$$

This implies that: (i) the corrector displacement vector at the probes is orthogonal to the predictor vector at the probes; or (ii) the probe points remain stationary in the corrector step ($\Delta \boldsymbol{u}_\mathrm{p}^{(j,k)} = \boldsymbol{0}$) such that the corrector is achieved by moving the main actuation point

only. Since only one independent probe is adopted here, case (ii) applies automatically as the predictor is naturally non-zero, *i.e.* $\Delta u_{\mathrm{p}}^{(1,k)} \neq 0$.

Conversely, if a large value of β is chosen, then the incremental displacement factor $\Delta\lambda^{(j,k)}$ is approximately equal to zero as the denominator in Eq. (19) dominates. In this case, the main actuation point remains stationary during the corrector increments and only the linked probes move, *i.e.* $\Delta u_{\mathrm{a}}^{(j,k)} = 0$ and $\Delta u_{\mathrm{p}}^{(j,k)} = -R_{\mathrm{p}}/K_{\mathrm{T}}^{\mathrm{pp}}$. This is essentially the same as the technique used in the simpler 'step-scan' method used by Neville *et al.* [22], where the actuation point remains stationary and the linked probes scan up and down to find a state that satisfies $R_{\mathrm{p}} = 0$. However, moving all control points (main actuation *and* probe points) in concert in the predictor step makes the current approach more efficient than the step-scan method, regardless of the choice of β.

During the experiments, it was found that the positional accuracy of the actuator attached to the probes was better than that of the actuator attached to the main actuation point. It was therefore beneficial for the current test setup to rely on the probes during corrective increments (*i.e.* large value of β). In the proximity of the limit point, however, the singularity of $K_{\mathrm{T}}^{\mathrm{pp}}$ implies that convergence difficulties are likely using this scheme. For example, large movements of the probes during corrective increments in the vicinity of the limit point can lead to snap-through of unrestrained portions of the arch. Moreover, as mentioned in Section Appendix B.2, the R_{p} *vs* u_{p} response during perturbation is not linear on the unstable path due to stick-slip in connections and manufacturing asymmetry of the arch. Corrective increments made by moving only the probes may be inefficient in this case due to the initial positive tangent (see Fig. Appendix B.2). Hence, corrector increments made by moving the main actuation point (small value of β) are more effective in this case.

In conclusion, due to the opposing requirements for large and small values of β, an adaptive scheme for varying β in the constraint condition was adopted. On the stable path, $\beta = 100$ and corrective increments rely primarily on moving the probes while the

actuation point remains stationary. When the magnitude of $K_{\mathrm{T}}^{\mathrm{pp}}$ becomes smaller than a threshold value, (currently 1.0 N/mm), β is set to zero. Only the main actuation point is then moved during the corrector increments while the probes remain stationary. Using this scheme, convergence problems caused by the singularity of $K_{\mathrm{T}}^{\mathrm{pp}}$ in the proximity of the limit point are avoided and the limit point can be traversed. For other test setups with different specifications for the main-actuation and probe-point actuator, the requirements on β may change.

Appendix B.4. Residual Probe Reaction Force following Perturbation

In computing the predictor step, the contribution to the incremental displacement from the residual R_{p} is normally assumed to be zero, because R_{p} needs to have fallen below a small tolerance for convergence of the previous load step. However, due to hysteresis and friction at connections, R_{p} can increase beyond the defined tolerance after the perturbation process to compute a new tangent stiffness matrix. This contribution $\mathrm{d}u_{\mathrm{p}}^{(1,k)}$ (defined in Eq. (12)) to the incremental displacement at the probes is of the same order of magnitude as the contribution of the tangent component $\Delta\lambda^{(1,k)}\delta u_{\mathrm{p}}^{(1,k)}$ (defined in Eq. (13)), particularly in the proximity of limit points and on the unstable path.

As noted in Section Appendix B.3, the corrective increments close to limit points rely on movements of the main actuation point. If R_{p} has shifted outside of the convergence tolerance during the perturbation process to compute $\boldsymbol{K}_{\mathrm{T}}^{\mathrm{p}}$, the resulting incorrect predictor at the probes is so significant that it cannot be corrected during the ensuing increments. Referring to Eq. (11), when the magnitude of $\mathrm{d}u_{\mathrm{p}}^{(1,k)}$ is larger than $\Delta\lambda^{(1,k)}\delta u_{\mathrm{p}}^{(1,k)}$ but of opposite sign, the probes move backwards to the preceding equilibrium configuration. Consequently, iterative non-converging loops in the incremental predictor-corrector process occur. Conversely, when the magnitude of $\mathrm{d}u_{\mathrm{p}}^{(1,k)}$ is smaller than $\Delta\lambda^{(1,k)}\delta u_{\mathrm{p}}^{(1,k)}$ but of opposite sign, the predictor at the probes is smaller than it should be. This leads to small incremental displacements for each step. Finally, if $\mathrm{d}u_{\mathrm{p}}^{(1,k)}$ is of the same sign as $\Delta\lambda^{(1,k)}\delta u_{\mathrm{p}}^{(1,k)}$, the predictor

is amplified, and this can lead to snap-through in unsupported sections of the arch.

To prevent these scenarios from occurring, the contribution from the residual reaction force at the probes after perturbation, $R_{\mathrm{p}}^{(1,k)}$, in the predictor increment $\Delta u_{\mathrm{p}}^{(1,k)}$ is excluded, *i.e.* $\Delta u_{\mathrm{p}}^{(1,k)} = \delta u_{\mathrm{p}}^{(1,k)} \Delta\lambda^{(1,k)}$. Thus, even though an unbalanced reaction force $R_{\mathrm{p}}^{(1,k)} > R_{\mathrm{p,tol}}$ might exist after perturbations, its effect on the predictor is ignored and assumed to be corrected through the subsequent increments.

Appendix B.5. Maximum Incremental Displacement

To prevent the arch specimen from physically breaking, limits on the maximum incremental displacement at the probes and the main actuation point must be set. Furthermore, an upper limit on the incremental displacement is essential to prevent the control points from overshooting beyond limit points. This is because a restart functionality, which works well in a numerical setting to restart the algorithm after a failed convergence attempt, is difficult to implement in an experimental setting due to hysteresis in the test setup.

For the arches tested herein (with $L_P = L/4$), limit points in the load-displacement response of the probes and the main actuation point, which correspond to changes in sign of $K_{\mathrm{T}}^{\mathrm{pa}}$ and $K_{\mathrm{T}}^{\mathrm{pp}}$, respectively, are closely spaced; see Fig. Appendix B.3. From Eq. (11), the predictor in the probes $\Delta \boldsymbol{u}_{\mathrm{p}}^{(1,k)}$ is given by

$$\Delta u_{\mathrm{p}}^{(1,k)} = -\frac{R_{\mathrm{p}} + K_{\mathrm{T}}^{\mathrm{pa}} \hat{u}_{\mathrm{a}} \Delta\lambda^{(1,k)}}{K_{\mathrm{T}}^{\mathrm{pp}}}. \tag{B.3}$$

In the proximity of limit points, $K_{\mathrm{T}}^{\mathrm{pp}}$ is close to zero, leading to a relatively large predictor $\Delta u_{\mathrm{p}}^{(1,k)}$. Overshooting in the probe displacement predictor cannot be corrected in the subsequent corrector increments and this leads to dynamic snaps in uncontrolled segments of the arch. Therefore, a fine incremental step size needs to be adopted. As the time efficiency of the experiment is poor if the maximum incremental step size is small, a varying tolerance scheme based on the magnitude of $K_{\mathrm{T}}^{\mathrm{pp}}$ and $K_{\mathrm{T}}^{\mathrm{pa}}$ is adopted. If $K_{\mathrm{T}}^{\mathrm{pp}}$ is smaller than a tolerance, here set at 1 N/mm, a relatively small value is adopted for the maximum displacement

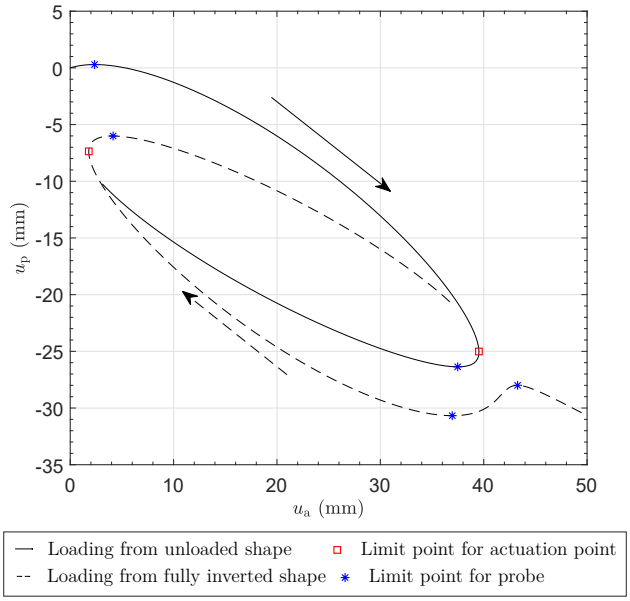

Figure Appendix B.3: Relationship between the actuation point and probe displacement for the arch with probe location $L_p = L/4$. Solid and dashed lines represent loading from the unloaded shape and fully inverted shape, respectively. The arrow represents the loading direction. Blue stars ($*$) and red squares ($\square$) represent limit points for u_p and u_a, respectively. Note that limit points for u_a and u_p correspond to tangent stiffness components $K_T^{pp} = 0$ and $K_T^{pa} = 0$, respectively.

limit. A relatively large value is adopted until the limit point of u_p is traversed, *i.e.* K_T^{pa} changes sign.

Appendix B.6. Predictor Direction Reversal at a Limit Point

In the current one-probe system, the condition to determine the predictor direction, *i.e.* Eq. (17), reduces to a product of two scalars. Thus, the direction reversal depends on the change of sign of the tangential probe displacement, $\delta u_p^{(1,k)}$. Referring to Eq. (13), the sign change in either K_T^{pa} or K_T^{pp} leads to this sign change in $\delta u_p^{(1,k)}$, *i.e.* a direction reversal in the predictor. Specifically, a reversal in the predictor direction of the actuation point occurs at all limit points presented in Fig. Appendix B.3. However, only the sign change in K_T^{pp} corresponds to a traversal of limit points in the main control point. To solve this

inconsistency, Eq. (17) is modified as follows

$$\begin{aligned}
&\textbf{if } K_{\mathrm{T}}^{\mathrm{pp}} \cdot K_{\mathrm{T}}^{\mathrm{pp,prev}} > 0 \text{ or } \Delta u_{\mathrm{p}}^{(\mathrm{k}-1)} \cdot \delta u_{\mathrm{p}}^{(1,k)} > 0 \\
&\quad \Delta\lambda^{(1,k)} = \|\Delta\lambda^{(1,k)}\| \\
&\textbf{else} \\
&\quad \Delta\lambda^{(1,k)} = -\|\Delta\lambda^{(1,k)}\|,
\end{aligned} \tag{B.4}$$

where $K_{\mathrm{T}}^{\mathrm{pp,prev}}$ is the tangent stiffness component of the preceding load step.

Appendix C. Modification of $\boldsymbol{K}_{\mathbf{T}}^{\mathbf{pa}}$ during Iteration Process

Before introducing the modification procedure, it is worth analysing the role of $K_{\mathrm{T}}^{\mathrm{pa}}$ during both the predictor and corrector process. We consider the cases of $\beta = 0$ and $\beta = 100$ separately.

For $\beta = 0$, if the forcing incremental factor of the predictor $\Delta\lambda^{(1,k)}$ is given by Eq. (15), then the predictor at the actuation point $\Delta u_{\mathrm{a}}^{(1,k)}$ is inversely proportional to $K_{\mathrm{T}}^{\mathrm{pa}}$, *i.e.* an under-estimated $K_{\mathrm{T}}^{\mathrm{pa}}$ leads to a larger predictor increment at the actuation point and *vice versa*. The magnitude of the probe predictor $\Delta u_{\mathrm{p}}^{(1,k)}$ is not affected by the sign of $K_{\mathrm{T}}^{\mathrm{pa}}$, but an incorrect sign points the predictor in the wrong direction. On the other hand, if $\Delta\lambda^{(1,k)}$ is given by Eq. (16), then the predictor $\Delta u_{\mathrm{a}}^{(1,k)}$ is not affected by $K_{\mathrm{T}}^{\mathrm{pa}}$, and $\Delta u_{\mathrm{p}}^{(1,k)}$ is proportional to $K_{\mathrm{T}}^{\mathrm{pa}}$. For correctors, the main actuation point is moved through $\Delta u_{\mathrm{a}}^{(j,k)} = -R_{\mathrm{p}}/K_{\mathrm{T}}^{\mathrm{pa}}$. If the approximated $K_{\mathrm{T}}^{\mathrm{pa}}$ is of the wrong sign, then the corrector moves in the wrong direction and thus the path-following process diverges. If the experimentally approximated $K_{\mathrm{T}}^{\mathrm{pa}}$ is overpredicted, then the path-following process converges at a slower rate with monotonically decreasing R_{p}. If the experimentally approximated $K_{\mathrm{T}}^{\mathrm{pa}}$ is under-predicted but larger than half of the 'actual' $K_{\mathrm{T}}^{\mathrm{pa}}$, *i.e.* the real stiffness, the path-following process converges with the magnitude of R_{p} decreasing monotonically but the sign of R_{p} changes from increment to increment. If the approximated $K_{\mathrm{T}}^{\mathrm{pa}}$ is equal to or less than half

of the 'actual' $K_{\mathrm{T}}^{\mathrm{pa}}$, the path-following process does not proceed, *i.e.* R_{p} jumps between positive and negative values in an endless loop.

For $\beta = 100$, $\Delta\lambda^{(1,k)}$ is given by Eq. (16). Therefore, $\Delta u_{\mathrm{a}}^{(1,k)}$ is not affected by $K_{\mathrm{T}}^{\mathrm{pa}}$. The predictor at the probes, $\Delta u_{\mathrm{p}}^{(1,k)}$, is proportional to $K_{\mathrm{T}}^{\mathrm{pa}}$. The corrector is achieved by moving the probes and the corresponding corrector is given by $-R_{\mathrm{p}}/K_{\mathrm{T}}^{\mathrm{pp}}$. An incorrect predictor is corrected during the corrector increments if the computed $\boldsymbol{K}_{\mathrm{T}}^{\mathrm{pp}}$ is of the correct sign. Therefore, $K_{\mathrm{T}}^{\mathrm{pa}}$ has no effect in such cases.

When the experimentally approximated $K_{\mathrm{T}}^{\mathrm{pa}}$ is grossly over- or underpredicted, a modification of the sign and magnitude of $K_{\mathrm{T}}^{\mathrm{pa}}$ can be made to avoid divergence. From the previous discussion it is known when $K_{\mathrm{T}}^{\mathrm{pa}}$ has been inaccurately approximated as the correctors will not move the arch closer to equilibrium; rather, the reaction forces on the probes increase. In general, two cases where $K_{\mathrm{T}}^{\mathrm{pa}}$ is incorrectly approximated are considered herein:

1. If the approximated $K_{\mathrm{T}}^{\mathrm{pa}}$ is of the opposite sign of the 'actual' value of $K_{\mathrm{T}}^{\mathrm{pa}}$, then the residual reaction force R_{p} increases monotonically as the iteration proceeds and path-following diverges.
2. If the approximated $K_{\mathrm{T}}^{\mathrm{pa}}$ is of the correct sign but its magnitude is less than half of the 'actual' value of $K_{\mathrm{T}}^{\mathrm{pa}}$, then the corrector is over-estimated and R_{p} changes sign from step to step in an endless loop.

To counteract these two scenarios, the flowchart in Fig. Appendix C.1 describes the subroutine that modifies the control algorithm.

References

[1] J. M. T. Thompson. Optimization as a generator of structural instability. *International Journal of Mechanical Sciences*, 14:627–629, 1972.

[2] R. M. J. Groh, D. Avitabile, and A. Pirrera. Generalised path-following for well-behaved nonlinear structures. *Computer Methods in Applied Mechanics and Engineering*, 331:394–426, 2018.

[3] P. M. Reis. A perspective on the revival of structural (in)stability with novel opportunities for function: From buckliphobia to buckliphilia. *Journal of Applied Mechanics*, 82(11):111001, 2015.

[4] R. L Harne and K. W. Wang. A review of the recent research on vibration energy harvesting via bistable systems. *Smart Materials and Structures*, 22:023001, 2013.

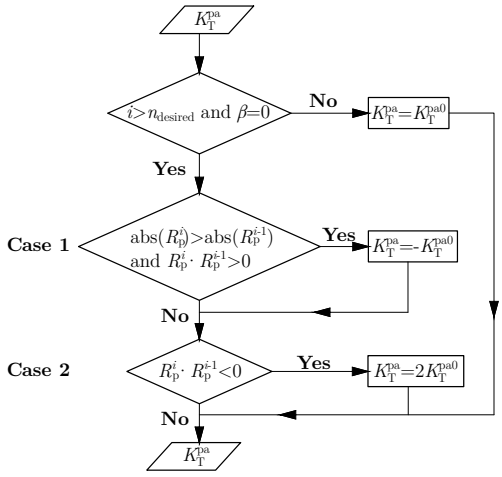

Figure Appendix C.1: Flowchart for the modification of K_T^{pa} based on the reaction force variation during the iteration procedure. Note that the modification is triggered only in the case where the number of iterations exceeds the desired number of iterations and the correctors are achieved by moving only the main actuation point.

[5] S. Emam and D. Inman. A review on bistable composite laminates for morphing and energy harvesting. *Applied Mechanics Reviews*, 67(6):060803, 2015.

[6] G. Arena, R. M. J. Groh, A. Brinkmeyer, R. Theunissen, P. M. Weaver, and A. Pirrera. Adaptive compliant structures for flow regulation. *Proceedings of the Royal Society A*, 473:20170334, 2017.

[7] M. Gomez, D. E. Moulton, and D. Vella. Passive control of viscous flow via elastic snap-through. *Physical Review Letters*, 119:144502, 2017.

[8] K. A. Seffen and S. V. Stott. Surface texturing through cylinder buckling. *Journal of Applied Mechanics*, 81:061001, 2014.

[9] J. T. B Overvelde, T. Kloek, J. J. A. D'haen, and K. Bertoldi. Amplifying the response of soft actuators by harnessing snap-through instabilities. *Proceedings of the National Academy of Sciences*, 112(35):10863–10868, 2015.

[10] J. Shim, C. Perdigou, R. E. Chen, K. Bertoldi, and P. M. Reis. Buckling-induced encapsulation of structured elastic shells under pressure. *Proceedings of the National Academy of Sciences*, 109(16):5978–5983, 2012.

[11] K. Bertoldi, P. M. Reis, S. Willshaw, and T. Mullin. Negative Poisson's ratio behavior induced by an elastic instability. *Advanced Materials*, 22:361–366, 2010.

[12] N. Hu and R. Burgueño. Tailoring the elastic postbuckling response of cylindrical shells: A route for exploiting instabilities in materials and mechanical systems. *Extreme Mechanics Letters*, 4:103–110, 2015.

[13] E. Riks. An incremental approach to the solution of snapping and buckling problems. *Journal of Solids and Structures*, 15:529–551, 1979.

[14] M. A. Crisfield. A fast incremental/iterative solution procedure that handles "snap-through". *Computers and Structures*, 13:55–62, 1981.

[15] A. Eriksson. Structural instability analyses based on generalised path-following. *Computer Methods in Applied Mechanics and Engineering*, 156:45–74, 1998.

[16] B. L. Wardle. Solution to the incorrect benchmark shell-buckling problem. *AIAA Journal*, 46(2):381–387, 2008.

[17] I. Leahu-Aluas and F. Abed-Meraim. A proposed set of popular limit-point buckling benchmark problems. *Structural Engineering and Mechanics*, 38(6):767–802, 2011.
[18] C. Thill, J. Etches, I. Bond, K. Potter, and P. M. Weaver. Morphing skins. *Aeronautical Journal*, 112:117–139, 2008.
[19] R. Wiebe and L. N. Virgin. On the experimental identification of unstable static equilibria. *Proceedings of the Royal Society A: Mathematical, Physical and Engineering Sciences*, 472(2190), 2016.
[20] E. Virot, T. Kreilos, T. M. Schneider, and S. M. Rubinstein. Stability landscape of shell buckling. *Physical Review Letters*, 119:224101, 2017.
[21] T. van Iderstein and R. Wiebe. Experimental path following of unstable static equilibria for snap-through buckling. In Gaetan Kerschen, editor, *Nonlinear Dynamics, Volume 1*, pages 17–22. Springer International Publishing, 2018.
[22] R. M. Neville, R. M. J. Groh, A. Pirrera, and M. Schenk. Beyond the fold: experimentally traversing limit points in nonlinear structures. *Proceedings of the Royal Society A*, 476:20190576., 2020.
[23] R. M. Neville, R. M. J. Groh, A. Pirrera, and M. Schenk. Shape control for experimental continuation. *Physical Review Letters*, 120(25):254101, 2018.
[24] J Sieber, A Gonzalez Buelga, SA Neild, DJ Wagg, and B Krauskopf. Experimental continuation of periodic orbits through a fold. *Physical Review Letters*, 100(244101):1 – 4, 6 2008. Publisher: American Physical Society.
[25] J. Sieber, B. Krauskopf, D. Wagg, S. Neild, and Alicia Gonzalez-Buelga. Control-based continuation of unstable periodic orbits. *Journal of Computational and Nonlinear Dynamics*, 6(1), 2011.
[26] F. Schilder, E. Bureau, I. Ferreira Santos, J. J. Thomsen, and J. Starke. Experimental bifurcation analysis—continuation for noise-contaminated zero problems. *Journal of Sound and Vibration*, 358:251–266, dec 2015.
[27] L. Renson, J. Sieber, D. A. W. Barton, A. D. Shaw, and S. A. Neild. Numerical continuation in nonlinear experiments using local gaussian process regression. *Nonlinear Dynamics*, 2019.
[28] L. Renson, D. A. W. Barton, and S. A. Neild. Experimental tracking of limit-point bifurcations and backbone curves using control-based continuation. *International Journal of Bifurcation and Chaos*, 27(01):1730002, jan 2017.
[29] J. Shen, R. M. J. Groh, M. Schenk, and A. Pirrera. Experimental path-following of equilibria using newton's method. part ii: Applications and outlook. *International Journal of Solids and Structures*, 2020. submitted.
[30] R. de Borst, M. A. Crisfield, J. J. C. Remmers, and C. V. Verhoosel. *Nonlinear Finite Element Analysis of Solids and Structures*. Wiley, 2 edition, 2012.
[31] D. C. Kammer. Sensor placement for on-orbit modal identification and correlation of large space structures. *J. Guid. Control Dyn.*, 14(2):251–259, 1991.
[32] D. C. Kammer. Optimal sensor placement for modal identification using system-realization methods. *J. Guid. Control Dyn.*, 19(3):729–731, 1996.
[33] M. Meo and G. Zumpano. On the optimal sensor placement techniques for a bridge structure. *Engineering Structures*, 27(10):1488–1497, 2005.
[34] A. Pirrera, R. M. J. Groh, J. Shen, and M. Schenk. Data for publication: Experimental path-following of equilibria using Newton's method. http://dx.doi.org/10.5523/bris.932lqv3akioz2jrwngdxzshfo.

Supplementary Material: Control parameter sensitivity study using the virtual testing environment

J. Shen, R. M. J. Groh, M. Schenk, A. Pirrera

In this document, we present a sensitivity study on the effects of primary controlling parameters and measurement noise on the convergence of the experimental continuation algorithm using the same circular shallow arch in Section 3.1 of the main text.

1 Residual Reaction Force Tolerance and Maximum Incremental Displacement Step Size

This section studies the effect of path-following parameters on the test set-up. The parameters varied are the residual reaction force tolerance $R_{\mathrm{p,tol}}$ and the maximum allowable incremental displacement step size $\Delta u_{\mathrm{a,max}}$ (*i.e.* a limit on the maximum change in the displacement of the main actuation point in one load step). The maximum incremental displacement step size plays an important role in determining how many corrector iterations are necessary for convergence. For example, when the incremental step size is sufficiently small, the solver may not require any corrector iterations at all.

The results for different reaction force tolerance and maximum allowable incremental step size values are presented in Fig. 1. In addition to the converged equilibria (blue squares), the predictor-corrector iterative solutions are also displayed (grey triangles). The solid line represents numerical results obtained using the quasi-static Riks solver in Abaqus (no probes) and can be treated as a benchmark solution. Compared to Fig. 6d in Section 3.1 of the main text, where we chose $R_{\mathrm{p,tol}} = 0.1\,\mathrm{N}$ and $\Delta u_{\mathrm{a,max}} = 0.001\,\mathrm{m}$, Fig. 1a shows that increasing $R_{\mathrm{p,tol}}$ and $\Delta u_{\mathrm{a,max}}$ leads to an increase in the incremental displacement step size while maintaining accuracy. By increasing $R_{\mathrm{p,tol}}$ further (see Fig. 1b), some equilibrium states start to diverge from the benchmark equilibrium curve. However, this divergence can be alleviated by decreasing $\Delta u_{\mathrm{a,max}}$, as shown in Fig. 1c. Increasing $R_{\mathrm{p,tol}}$ even further while keeping $\Delta u_{\mathrm{a,max}}$ fixed (see Fig. 1d), the path-following process eventually fails to traverse the displacement limit point and the arch snaps to another equilibrium configuration. This problem can be alleviated by decreasing $\Delta u_{\mathrm{a,max}}$ manually in the proximity of the displacement limit point.

In conclusion, less stringent reaction force tolerance values can be balanced by decreasing the maximum incremental displacement step size. This observation suggests that if the force sensors on the probes have poor measurement accuracy, then the incremental

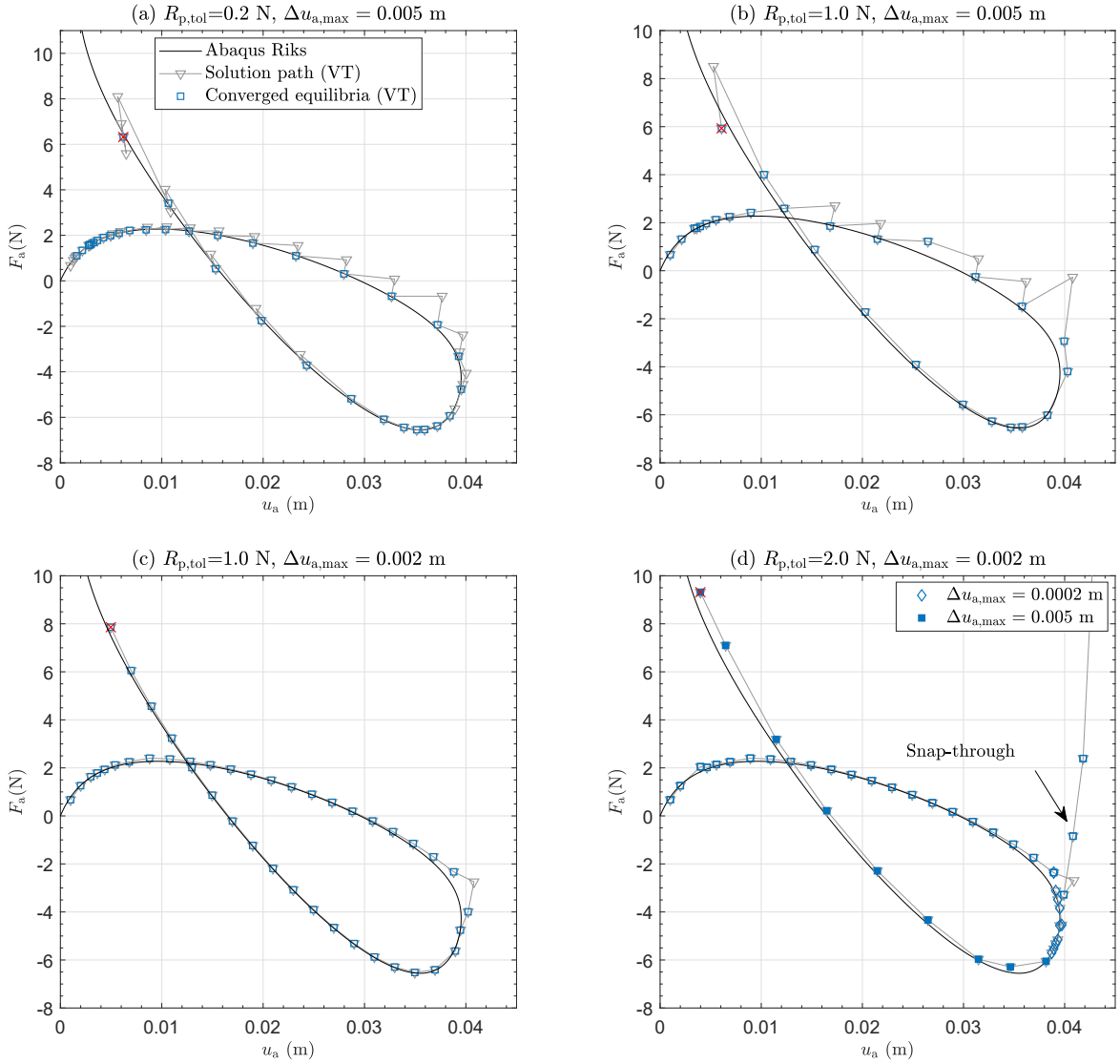

Figure 1: The effects of the residual reaction force tolerance $R_{\mathrm{p,tol}}$ and maximum actuation point incremental step size $\Delta u_{\mathrm{a,max}}$ on the path-following procedure for one probe pair located at $L_{\mathrm{p}} = L/4$. Grey triangles represent the predictor-corrector solution process, while blue squares are converged equilibria. The solid line represents numerical results obtained using the standard Riks solver in ABAQUS (no probes).

displacement step size should be reduced accordingly. There is, of course, a limit to how small displacement increments can be, due to limitations on actuator precision and backlash in components. Thus, a compromise needs to be established between probe force sensor accuracy and displacement actuator precision.

Further trade-offs concern the total duration of an experiment, achieving a balance between the time required to compute the tangent stiffness and to execute the subsequent predictor-corrector steps. For the modified Newton approach used herein, the tangent stiffness matrix is only computed at the beginning of each load step, which requires N_p perturbations for N_p independent probe points. When small $\Delta u_{\mathrm{a,max}}$ are adopted, convergence is often reached within the predictor step. However, this approach may be less efficient than having larger values of $\Delta u_{\mathrm{a,max}}$, even though the latter requires several corrector steps to reach convergence. In our experience, large $\Delta u_{\mathrm{a,max}}$ values require less time for the experimental set-up to trace the whole equilibrium path, as fewer computations of the tangent stiffness matrix are made. Thus, $\Delta u_{\mathrm{a,max}}$ should be kept as large as possible unless convergence problems are encountered.

2 Noise and Measurement Uncertainty

In Sections 3.1 and 3.2 of the main text, experimental noise and measurement uncertainty in the force and displacement measurements were ignored. Stochastic variations and measurement uncertainties will, however, affect any experimental set-up. The virtual testing environment enables us to explore the effects of noise and uncertainty on the experimental setup, which can consequently be designed for robustness. For the sake of brevity, in this section, we consider only the test case with one pair of probes located at $L_\mathrm{p}/L = 1/4$.

Noise and measurement uncertainty can be modelled in the virtual testing environment by perturbing the displacements and reaction forces using a random number generator. One option is to incorporate noise in the following way

$$\boldsymbol{u}_{\mathrm{real}} = \boldsymbol{u}_{\mathrm{ideal}} + \boldsymbol{u}_{\mathrm{error}}, \qquad \boldsymbol{R}_{\mathrm{real}} = \boldsymbol{R}_{\mathrm{ideal}} + \boldsymbol{R}_{\mathrm{error}}, \tag{1}$$

where the subscripts $\bullet_{\mathrm{real}}$, $\bullet_{\mathrm{ideal}}$ and $\bullet_{\mathrm{error}}$ represent, respectively: the data measured and used in the controlling algorithm; the idealised control signals (zero-noise measurements); and the noise or error in the data measurement system. The noise (error) is assumed to follow a normal Gaussian distribution, modelled using the function NUMPY.RANDOM.NORMAL in PYTHON.

From the sensitivity analysis on the residual tolerance values $R_{\mathrm{p,tol}}$ presented in Section 1, we infer that the impact of noise on the reaction force measurements should be small as increasing the tolerance in Section 1 did not have a significant effect on the converged equilibria. However, noise can have significant effects on the experimental tangent stiffness $\boldsymbol{K}_\mathrm{T}^\mathrm{p}$. In the presence of noise in the force measurements, tangent stiffness terms are approximated by finite differences as

$$K_\mathrm{T}^{p,ij} = \frac{(R_{\mathrm{p},i}(u_j + \Delta u_j) - R_{\mathrm{p},i}(u_j)) + R_{\mathrm{p,err},i}}{\Delta u_j}. \tag{2}$$

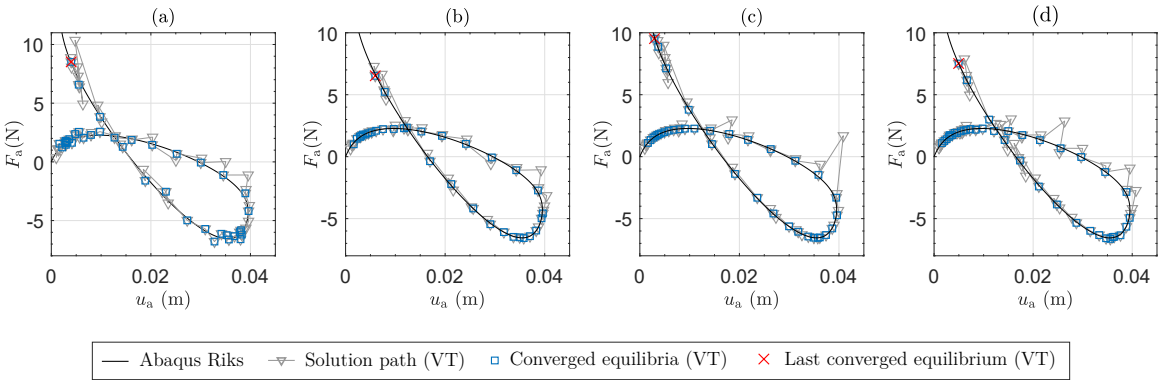

Figure 2: Effects of noise in the force signals and uncertainty in the enforced displacements on the virtual testing results. Sub-figures (a) and (b) only consider noise in the force measurement with reaction forces at the probes measured (a) only once, and (b) 20 times with the average adopted as the 'actual' force in the controlling algorithm. (c) Uncertainty only in the displacement enforced by actuators. (d) Noise in the force measurement system as well as uncertainty in the displacements, where the force reading is averaged over 20 measurements. The standard deviation in the force and displacement measurements are obtained from (0) with values of 0.0014 N and 0.0016 mm for the actuation point, and 0.1155 N and 0.0065 mm for the probes, respectively.

When the noise in the reaction force measurement is of the same order of magnitude as the changes in the measured reaction force on the probes, *i.e.* $\mathcal{O}(R_{\mathrm{p,err},i}) = \mathcal{O}(R_{\mathrm{p},i}(u_j + \Delta u_j) - R_{\mathrm{p},i}(u_j))$, large errors in the approximation of $K_{\mathrm{T}}^{p,ij}$ are to be expected.

In this section, virtual testing analyses are run with noise values based on previous experimental work with the same equipment (0). The standard deviation in the force and displacement measurements are taken as 0.0014 N and 0.0016 mm for the actuation point, and 0.1155 N and 0.0065 mm for the probes, respectively. All other parameters remain as in previous sections. Figure 2a shows results with added noise when the tangent stiffness matrix is determined by perturbing each probe only once. Severe zig-zagging in the equilibrium curve is observed just after the limit point because $K_{\mathrm{T}}^{\mathrm{pp}}$ is close to singular. Due to the singularity, noise has a relatively large effect on $K_{\mathrm{T}}^{\mathrm{pp}}$, making convergence difficult. In other regions of the equilibrium curve, the algorithm converges well despite the addition of noise.

By measuring the reaction force at each probe 20 times, *i.e.* for 20 nominally identical probe perturbations, and passing average tangent stiffness terms to the controlling algorithm, the zig-zagging in the equilibrium path observed in Fig. 2a disappears. These results are shown in Fig. 2b, where the equilibrium manifold is similar to that obtained without noise. It is therefore recommended that multiple measurements of the probe forces are taken and an averaged value used in the control algorithm. While this procedure will reduce the effects of uncorrelated (white) noise, correlated (systemic) noise due to inaccura-

cies in the measurement devices will not be remedied by this approach. Moreover, multiple measurements decrease experimental efficiency and may introduce systematic errors due to material creep and other hysteresis effects.

The results for uncertainties in the enforced displacements are presented in Fig. 2c. Compared with noise in the probe force measurements (see Fig. 2a), the effect of uncertainty in the displacement actuators on the equilibrium path is less significant (Fig. 2c). Finally, Fig. 2d presents a combination of noise in the force readings (measuring reaction forces 20 times) and uncertainty in the enforced displacements. Converged equilibria are close to those shown in Fig. 2b.

3 Perturbation Size and Experimental Tangent Stiffness Matrix

To reduce the effect of noise on the accuracy of $\boldsymbol{K}_{\mathrm{T}}^{\mathrm{p}}$, we increase the displacement perturbation Δu_j so that $\|R_{\mathrm{p},i}(u_j+\Delta u_j)-R_{\mathrm{p},i}(u_j)\|_2 \gg \|R_{\mathrm{p,err,i}}\|_2$ (see Eq. (2)). However, a large perturbation size can also lead to an inaccurate computation of $\boldsymbol{K}_{\mathrm{T}}^{\mathrm{p}}$ as finite differences—being derived from linear approximations of derivatives—typically rely on small perturbations. Therefore, a sensitivity study on the perturbation size is conducted here. Figure 3 presents the virtual testing results of $\boldsymbol{K}_{\mathrm{T}}^{\mathrm{p}}$ for different displacement perturbations Δu_j. All perturbation sizes allow traversal of the first displacement limit point in the equilibrium manifold. However, all other parameters being equal, a smaller perturbation size generally leads to fewer corrector iterations. Due to the automatic step size incrementation rule of Eq. (16), smaller perturbations therefore facilitate larger incremental step sizes. It should also be noted that the results presented in Fig. 3a are identical to those in Fig. 1a, even though the perturbation size in the latter case is ten times larger. This implies that there exists a lower-bound threshold for the perturbation size below which $\boldsymbol{K}_{\mathrm{T}}^{\mathrm{p}}$ is not affected.

References

R. M. Neville, R. M. J. Groh, A. Pirrera, and M. Schenk. Shape control for experimental continuation. *Physical Review Letters*, 120(25):254101, 2018.

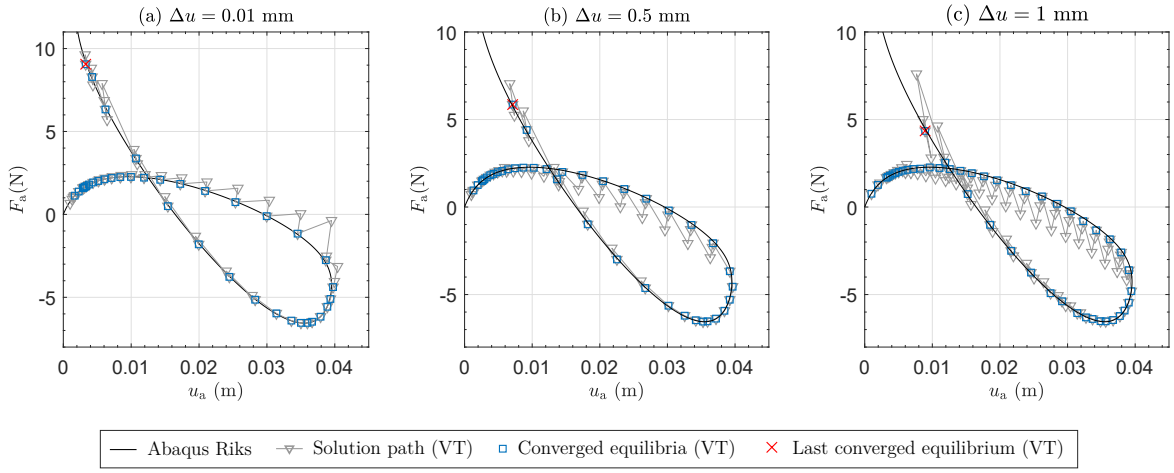

Figure 3: Virtual testing on the shallow arch with different perturbations Δu in approximating the experimental tangent stiffness matrix $\boldsymbol{K}_{\mathrm{T}}^{\mathrm{p}}$. Note that the tolerance for residual reaction force, $R_{\mathrm{p,tol}}$, and maximum incremental displacement step size at the actuation point, $\Delta u_{\mathrm{a,max}}$, are the same as in Fig. 1a. Noise in the displacement and force measurement is excluded in all cases.